

The dynamics of three nearby E0 galaxies in refracted gravity

V. Cesare^{1,2}, A. Diaferio^{1,2}, and T. Matsakos¹

¹ Dipartimento di Fisica, Università di Torino, via P. Giuria 1, 10125, Torino, Italy, e-mail: valentina.cesare@unito.it

² Istituto Nazionale di Fisica Nucleare (INFN), Sezione di Torino, Torino, Italy

Received <date> / Accepted <date>

ABSTRACT

We test whether refracted gravity (RG), a modified theory of gravity that describes the dynamics of galaxies without the aid of dark matter, can model the dynamics of the three massive elliptical galaxies, NGC 1407, NGC 4486, and NGC 5846, out to $\sim 10R_e$, where the stellar mass component fades out and dark matter is required in Newtonian gravity. We probe these outer regions with the kinematics of the globular clusters provided by the SLUGGS survey. RG mimics dark matter with the gravitational permittivity, a monotonic function of the local mass density depending on three parameters, ϵ_0 , ρ_c , and Q , that are expected to be universal. RG satisfactorily reproduces the velocity dispersion profiles of the stars and red and blue globular clusters, with stellar mass-to-light ratios in agreement with stellar population synthesis models, and orbital anisotropy parameters consistent with previous results obtained in Newtonian gravity with dark matter. The sets of three parameters of the gravitational permittivity found for each galaxy are consistent with each other within $\sim 1\sigma$. We compare the mean ϵ_0 , ρ_c , and Q found here with the means of the parameters required to model the rotation curves and vertical velocity dispersion profiles of 30 disk galaxies from the DiskMass survey (DMS): ρ_c , and Q are within 1σ from the DMS values, whereas ϵ_0 is within 2.5σ from the DMS value. This result suggests the universality of the permittivity function, despite our simplified galaxy model: we treat each galaxy as isolated, when, in fact, NGC 1407 and NGC 5846 are members of galaxy groups and NGC 4486 is the central galaxy of the Virgo cluster.

Key words. Gravitation - Galaxies: kinematics and dynamics - Galaxies: individual: NGC 1407, NGC 4486, NGC 5846 - Dark matter - Surveys - Methods: statistical

1. Introduction

The observed kinematical properties of the luminous matter in galaxies suggest that $\sim 80 - 90\%$ of the mass of the galaxies is dark (Del Popolo 2014). This result consistently fits within the standard cosmological model, where the properties of the Universe on large scales, including the temperature anisotropies of the cosmic microwave background (CMB) (Planck Collaboration et al. 2020), the large-scale distribution of galaxies (Dodelson et al. 2002) and the abundance of light elements (Cyburt et al. 2016) imply that the matter content of the Universe is dominated by cold dark matter.

The standard cosmological model, however, suffers from some tensions both on large scales and on the scale of galaxies. On large scales, the discrepancy between the value of the Hubble constant, H_0 , derived from observations in the local Universe and the value derived from the CMB (Verde et al. 2019), the unlikely features in the CMB temperature anisotropies (Schwarz et al. 2016), and the deficiency of ${}^7\text{Li}$ (Mathews et al. 2020) have recently challenged the standard model. On the scale of galaxies, the tensions have been long-lasting: in disk galaxies, fine-tuned interactions between baryonic and dark matter are necessary to describe the radial acceleration relation or the baryonic Tully-Fisher relation (McGaugh 2020); the missing satellite problem, the plane of satellite galaxies around the Milky Way, and the cusp-core problem in dwarf galaxies pose additional challenges (see e.g. Kroupa 2012; Del Popolo & Le Delliou 2017; de Martino et al. 2020, for reviews). Moreover, the search for the elementary particles constituting the dark matter remains inconclusive (Tanabashi et al. 2018).

On the scale of galaxies, a number of models beyond the standard model have been suggested. Dark matter particles might not be cold and collisionless, but rather self-interacting (Tulin & Yu 2018), fuzzy (Hui et al. 2017), axion-like (Marsh 2016), or a superfluid (Ferreira et al. 2019). Alternatively, the theory of gravity might break down on galaxy and larger cosmic scales and dark matter might thus be unnecessary. Modified gravity theories proposed in the literature are numerous: for example, $f(R)$ gravity, where the Ricci scalar R in the Einstein-Hilbert action is replaced by an arbitrary function of R (Nojiri & Odintsov 2011) or conformal gravity, where R is replaced by the contraction of the fourth-rank Weyl tensor (Mannheim 2019). However, both modified dark matter models and modified gravity theories have encountered a number of challenges. For example, neither $f(R)$ nor conformal gravity appear to be able to yield the correct abundance of light elements (Azevedo & Avelino 2018; Elizondo & Yepes 1994). Conformal gravity also appears to suffer from a severe fine tuning in the description of the kinematics of disk galaxies (Campigotto et al. 2019) and requires a too hot intergalactic medium in galaxy clusters (Horne 2006; Diaferio & Ostorero 2009). Modified Newtonian dynamics (MOND) has been proved to be the most successful phenomenological model on the scale of galaxies (Sanders & McGaugh 2002; McGaugh 2020), but attempts to build a covariant formulation of MOND remain challenging (Famaey & McGaugh 2012; Milgrom 2015; Hernandez et al. 2019).

Matsakos & Diaferio (2016) suggested Refracted Gravity (RG), a theory of gravity where the Poisson equation is modified by the introduction of the gravitational permittivity, a monotonic increasing function of the local mass density. RG appears

to properly describe the observed phenomenology on the scale of galaxies and clusters of galaxies, with the role of dark matter mimicked by the gravitational permittivity (Matsakos & Diaferio 2016; Cesare et al. 2020). In addition, RG provides a straightforward covariant extension within the family of the scalar-tensor theories (Sanna et al., in preparation). In the covariant-tension, the role of the gravitational permittivity is played by the scalar field. This same scalar field is also responsible for the accelerated expansion of the Universe. Thus, RG has the attractive feature of unifying the two dark sectors of the Universe into a single scalar field (Carneiro 2018; Bertacca et al. 2010).

In the weak-field limit, RG has two distinctive properties: in flat systems, like disk galaxies, the gravitational permittivity bends the lines of the gravitational field towards the system, thus determining a boost of the gravitational field in the plane perpendicular to the minor axis of the system. In spherically symmetric systems, the field lines remain radial, but the gravitational field is enhanced by the inverse of the gravitational permittivity. In Cesare et al. (2020), we investigate the dynamics of 30 disk galaxies from the DiskMass Survey (DMS, Bershady et al. 2010). These galaxies are almost face-on and they thus enable the measurements of both the rotation curve and the profile of the stellar velocity dispersion perpendicular to the plane of the disk. Cesare et al. (2020) prove that the bending of the gravitational field lines occurring in RG is sufficient to describe the kinematics of these 30 DMS galaxies without resorting to dark matter. This description depends on three parameters appearing in the gravitational permittivity. A single set of parameters describes the entire sample of 30 galaxies, supporting the expectation that these parameters should be universal. These encouraging results on flat systems motivate us to test whether RG is also able to describe the dynamics of spherical systems with the same set of parameters. In other words, we wish to probe that the boost of the gravitational field can be set by the gravitational permittivity alone, independently of the redirection of the field lines.

Here, we illustrate the result of this test on three E0 galaxies, that are approximately spherical. We consider NGC 1407, NGC 4486, alias M87, and NGC 5846 from the SLUGGS survey¹ (Pota et al. 2013; Brodie et al. 2014; Forbes et al. 2017). In elliptical galaxies, the baryonic matter within $1R_e$, the effective radius at half projected luminosity, suffices to describe the galaxy dynamics with Newtonian gravity (e.g. Dekel et al. 2005; Mamon & Łokas 2005; Proctor et al. 2009; Cappellari et al. 2013). To probe RG, we thus need kinematic information in the outer regions, where Newtonian gravity breaks down unless dark matter is assumed to exist. X-ray emitting gas, planetary nebulae, and globular clusters (GCs) have been adopted as kinematic tracers in these regions, out to $\sim 10R_e$, where the stellar luminosity fades out (Danziger 1997; Mathews & Brighenti 2003; Werner et al. 2019; Pota et al. 2013; Pulsoni et al. 2018). In addition, GCs usually appear separated into two distinct populations, according to their colour. Red GCs are generally more spatially concentrated and have smaller velocity dispersions than blue GCs (Geisler et al. 1996; Ashman & Zepf 1998; Bassino et al. 2006; Brodie & Strader 2006; Faifer et al. 2011; Strader et al. 2011; Forbes et al. 2012; Lee et al. 2008; Pota et al. 2013). By adopting GCs as tracers of the velocity field in the outer regions of ellipticals, we thus actually have two tracers rather than one and they can thus more strongly constrain the model. The SLUGGS survey provides the ideal dataset for our test of RG.

Studying the outer regions of ellipticals might be, however, particularly insidious. Here, we will model each galaxy as an

isolated system. However, ellipticals tend to live in dense environments: NGC 1407 and NGC 5846 are within groups and NGC 4486 is the central galaxy of the Virgo cluster. Therefore, their outer regions are subject to the gravitational field of nearby galaxies and of the hosting system as a whole. Nevertheless, we will see that our RG model can satisfactorily describe the overall dynamics of these elliptical galaxies.

Section 2 summarises the main features of RG. Sections 3 and 4 describe the photometric and spectroscopic data that we use in our analysis. In Sect. 5, we illustrate our RG dynamical model, and in Sect. 6 we report our results. We conclude in Sect. 7. We adopt a Hubble constant $H_0 = 73 \text{ km s}^{-1} \text{ Mpc}^{-1}$ (Riess et al. 2016) throughout the paper.

2. Refracted gravity

RG is a classical theory of modified gravity where dark matter is mimicked by a gravitational permittivity, $\epsilon(\rho)$, a monotonic increasing function of the local mass density ρ . The gravitational permittivity appears in the modified Poisson equation

$$\nabla \cdot [\epsilon(\rho)\nabla\phi] = 4\pi G\rho, \quad (1)$$

where ϕ is the gravitational potential and G the gravitational constant; the permittivity $\epsilon(\rho)$ has the asymptotic values

$$\epsilon(\rho) = \begin{cases} 1, & \rho \gg \rho_c \\ \epsilon_0, & \rho \ll \rho_c, \end{cases} \quad (2)$$

where $0 < \epsilon_0 \leq 1$ is the gravitational permittivity in vacuum and ρ_c is a critical density.

According to Eqs. (1) and (2), when the density is much larger than ρ_c , we recover the Newtonian Poisson equation $\nabla^2\phi = 4\pi G\rho$. On the contrary, in low-density regions, the gravitational permittivity enhances the gravitational field. RG predicts a different behaviour for the gravitational field in spherical and flattened systems. For spherical systems, the integration of Eq. (1) yields

$$\frac{d\phi}{dr} = \frac{GM(r)}{\epsilon(\rho)r^2}, \quad (3)$$

where $M(r)$ is the total mass of the system within radius r . The RG gravitational field has the same direction and r -dependence as in the Newtonian case, but it is enhanced by the inverse of the permittivity.²

For flat systems, the lines of the gravitational field are focussed towards the mid-plane of the source: the expansion of the divergence of Eq. (1),

$$\frac{\partial\epsilon}{\partial\rho}\nabla\rho \cdot \nabla\phi + \epsilon(\rho)\nabla^2\phi = 4\pi G\rho, \quad (4)$$

² Equation (3) shows that the gravitational field is $\propto r^{-2}$ in the vacuum, where both $M(r)$ and $\epsilon(\rho)$ are constant. This behaviour of the RG gravitational field does not necessarily contradict the observed velocity dispersion profiles of elliptical galaxies (Jiménez et al. 2013; Durazo et al. 2017, 2018) and of GCs (Hernandez & Jiménez 2012; Hernandez et al. 2013a; Durazo et al. 2017; Hernandez & Lara-D I 2020), or the external $\rho \propto r^{-3}$ mass density profiles of spherical stellar systems (Hernandez et al. 2013b) that suggest a gravitational field falling off as r^{-1} . No astrophysical system is completely isolated and exactly satisfies the conditions $M(r) = \text{const}$ and $\epsilon(\rho) = \text{const}$ in its outer regions. Therefore, in principle, the permittivity $\epsilon(\rho)$ can determine an r^{-1} behaviour of the gravitational field in each of these systems depending on the actual density field of its environment.

¹ <https://sluggs.swin.edu.au/Start.html>

shows that the gravitational potential ϕ depends on both the density ρ and on its variation $\nabla\rho$. RG predicts that, when interpreted in Newtonian gravity, the flatter the system, the larger its mass discrepancy, because the redirection of the field lines increases with the flatness of the source. This prediction might be consistent with the claimed correlation between the dark matter content of elliptical galaxies and their ellipticity (Deur 2014, 2020). Similarly, although it still requires a quantitative confirmation, this prediction might also be connected with the different dark matter content of dwarf galaxies and GCs: albeit of similar stellar mass, the dwarfs are spheroidal and dark matter-dominated in Newtonian gravity, whereas the GCs are spherical and devoid of dark matter (e.g. Strigari et al. 2008; Sollima & Nipoti 2010).

In this work, we solve Eq. (3) for three approximately spherical galaxies to determine whether the gravitational permittivity can describe the dynamics of spherical systems independently of the redirection of the field lines. In Eq. (3), the mass density ρ and, consequently, the cumulative mass profile $M(r)$ of each galaxy are associated with the baryonic matter alone. For the gravitational permittivity, according to Matsakos & Diaferio (2016) and Cesare et al. (2020), we adopt the smooth step function

$$\epsilon(\rho) = \epsilon_0 + (1 - \epsilon_0) \frac{1}{2} \left\{ \tanh \left[\ln \left(\frac{\rho}{\rho_c} \right)^Q \right] + 1 \right\}. \quad (5)$$

Q regulates the steepness of the transition between the Newtonian and the RG regimes: the larger Q , the steeper the transition. With this formulation, RG has three free parameters that we expect to be universal: ϵ_0 , ρ_c , and Q .

3. Photometric data

In this section, we describe the observables that enter our mass model of each galaxy: the surface brightness of the stars, the surface number densities of the GCs populations, the mass density of the hot X-ray emitting gas, and the mass of the central supermassive black hole (SMBH). Table 1 lists the quantities characterising the three galaxies and the colour cut that we adopt in Sect. 4.2 to separate the GC samples into the red and blue populations.

NGC 1407, NGC 4486, and NGC 5846 are at redshift $z < 0.007$. We can thus neglect any k -correction in the photometric measures and in the distance modulus $m - M = 5 \log_{10}[D(\text{pc})] - 5$, with m and M the apparent and absolute magnitudes of the source. Similarly, to convert the radial coordinate R projected on the sky from angular units, in arcsec, to physical units, in kpc, we adopt the relation, valid in a non-expanding Euclidean geometry,

$$R(\text{kpc}) = 4.84814 \times 10^{-6} D(\text{kpc}) R(\text{arcsec}), \quad (6)$$

with D the distance to the galaxy. For elliptical galaxies, the radial coordinate R is

$$R = \sqrt{qx^2 + \frac{y^2}{q}}, \quad (7)$$

where q is the minor-to-major axis ratio of the galaxy on the sky, and the x' and y' coordinates are oriented along the galaxy major and minor axes, respectively (e.g. Cappellari 2008; Cappellari et al. 2013; Napolitano et al. 2009; Pota et al. 2013, 2015).

3.1. Stellar surface brightness profiles

For the surface brightness of the stars, we adopt the models derived by Pota et al. (2015) for NGC 1407 and by Scott et al. (2013) for NGC 4486 and NGC 5846.

3.1.1. NGC 1407

The stellar surface brightness profile of NGC 1407 is measured in the B -band with the *Hubble Space Telescope*/ACS (Spolaor et al. 2008; Rusli et al. 2013) and in the g -band with the Subaru/Suprime-Cam (Pota et al. 2013). The B and g -bands largely overlap; therefore, Pota et al. (2015) derive a unique surface brightness profile in the B -band by a proper transformation of the g -band data. NGC 1407 has ellipticity $\varepsilon = 1 - q = 0.05$. Pota et al. (2015) model the surface brightness profile with the Sérsic profile

$$I_*(R) = I_e \exp \left\{ -b_{n_s} \left[\left(\frac{R}{R_e} \right)^{\frac{1}{n_s}} - 1 \right] \right\}, \quad (8)$$

where the effective radius R_e encloses half of the total luminosity of the stellar distribution, I_e is the surface brightness at radius R_e , n_s is the Sérsic index, and

$$b_{n_s} = 2n_s - \frac{1}{3} + \frac{4}{405n_s} + \frac{46}{25515n_s^2} \quad (9)$$

(Ciotti & Bertin 1999). After deconvolving for the seeing, Pota et al. (2015) derive $R_e = (100 \pm 3)$ arcsec, $I_e = 3.5 \times 10^5 L_{\odot,B}$ arcsec $^{-2}$, and $n_s = 4.67 \pm 0.15$.

3.1.2. NGC 4486 and NGC 5846

Scott et al. (2013) measure the surface brightness of NGC 4486 and NGC 5846 in the $ugriz$ bands from the Sloan Digital Sky Survey DR7 (Abazajian et al. 2009) and the Wide Field Camera on the 2.5-m Isaac Newton Telescope at the Roque de los Muchachos observatory. Scott et al. (2013) model the two-dimensional map of the surface brightness in the r -band; this band reduces the dust contamination and provides images with the optimal signal-to-noise value (Cappellari et al. 2013). They adopt the axisymmetric Multi-Gaussian Expansion (MGE) approach (Emsellem et al. 1994), which yields the surface brightness map (Cappellari 2008; Cappellari et al. 2013)

$$I_*(x', y') = \sum_{k=1}^N \frac{L_k}{2\pi\sigma_k^2 q'_k} \exp \left[-\frac{1}{2\sigma_k^2} \left(x'^2 + \frac{y'^2}{q'_k} \right) \right], \quad (10)$$

where N is the number of Gaussian components in the MGE fit, and L_k , σ_k , and $0 \leq q'_k \leq 1$ are the luminosity, the standard deviation along the major axis, and the observed minor-to-major axis ratio of each Gaussian, respectively; x' and y' are the coordinates on the plane of the sky, where the x' -axis is oriented along the major axis of the galaxy. Scott et al. (2013) find $q'_k = 1$ within 5% for all the Gaussians of the model of each galaxy. Indeed, NGC 4486 has ellipticity $\varepsilon = 1 - q = 0.14$, and NGC 5846 has $\varepsilon = 0.08$. We thus model these galaxies as spherical systems, set $q'_k = 1$ for all the Gaussians, and adopt the parameters L_k and σ_k determined by Scott et al. (2013) for Eq. (10) in the surface brightness profile (Cappellari 2008)

$$I_*(R) = \sum_{k=1}^N \frac{L_k}{2\pi\sigma_k^2} \exp \left(-\frac{R^2}{2\sigma_k^2} \right). \quad (11)$$

Table 1: General properties of NGC 1407, NGC 4486, and NGC 5846.

NGC	D [Mpc]	z	q	N_{GCs}	$N_{\text{GCs,Blue}}$	$N_{\text{GCs,Red}}$	V_{hel} [km s^{-1}]	$(g-i)_{\text{TH}}$
(1)	(2)	(3)	(4)	(5)	(6)	(7)	(8)	(9)
1407	28.05	0.0068	0.95	379	153	148	1779 ± 9	0.98
4486	17.2	0.0042	0.86	737	480	199	1284 ± 5	0.93
5846	24.2	0.0059	0.92	195	91	102	1712 ± 5	0.95

Notes. Column 1: galaxy name; Col. 2: distance; Col. 3: redshift; Col. 4: minor-to-major axis ratio; Col. 5: number of confirmed GCs; Cols. 6–7: number of blue and red GCs in the final sample (see text). Col. 8: heliocentric velocity; Col. 9: $(g-i)$ colour threshold separating the GC population. The distance and the number of confirmed GCs of NGC 1407 are from Pota et al. (2015), whereas the distance and the number of confirmed GCs of NGC 4486 and NGC 5846 are from Pota et al. (2013). The number of blue and red GCs of NGC 1407 are from Pota et al. (2015), whereas the number of blue and red GCs of NGC 4486 and NGC 5846 are determined from our analysis. The minor-to-major axis ratio and the heliocentric velocities of the three galaxies are from Pota et al. (2013), as well as the $(g-i)$ colour thresholds for NGC 1407 and NGC 5846. The $(g-i)$ colour threshold for NGC 4486 is from Strader et al. (2011).

Scott et al. (2013) find $N = 9$ and $N = 7$ Gaussian components for NGC 4486 and NGC 5846, respectively. Tables 2 and 3 list L_k and σ_k after deconvolving for the seeing. Finally, the total stellar luminosity of the galaxy is (Cappellari et al. 2013)

$$L_{*,\text{tot}} = \sum_{k=1}^N L_k. \quad (12)$$

3.1.3. Stellar 3D luminosity density profiles

For NGC 1407, the three-dimensional (3D) luminosity density of the stars is the Abel integral, valid in spherical symmetry,

$$v_*(r) = -\frac{1}{\pi} \int_r^{+\infty} \frac{dI_*}{dR} \frac{dR}{\sqrt{R^2 - r^2}}, \quad (13)$$

where $I_*(R)$ is given by Eq. (8) and r is the radial coordinate in three dimensions. For NGC 4486 and NGC 5846, the deprojected MGE 3D luminosity density is (Cappellari 2008)

$$v_*(r) = \sum_{k=1}^N \frac{L_k}{(\sqrt{2\pi}\sigma_k)^3} \exp\left(-\frac{r^2}{2\sigma_k^2}\right). \quad (14)$$

The 3D luminosity density of the stars, $v_*(r)$, yields the stellar luminosity profile

$$L_*(r) = 4\pi \int_0^r v_*(r') r'^2 dr'. \quad (15)$$

The total stellar luminosity, $L_{*,\text{tot}}$, is formally obtained by setting $r = \infty$. However, $L_*(r)$ rapidly converges to $L_{*,\text{tot}}$. By setting $R = 4800$ arcsec, we obtain $L_*(R) = 8.51 \times 10^{10} L_{\odot}$ for NGC 1407, $L_*(R) = 7.39 \times 10^{10} L_{\odot}$ for NGC 4486, and $L_*(R) = 4.59 \times 10^{10} L_{\odot}$ for NGC 5846. These total luminosities are consistent with the total galaxy luminosities $L_{*,\text{tot}} = 8.53 \times 10^{10} L_{\odot}$, found by Pota et al. (2015) for NGC 1407, and $L_{*,\text{tot}} = 7.40 \times 10^{10} L_{\odot}$ and $L_{*,\text{tot}} = 4.62 \times 10^{10} L_{\odot}$, found by Scott et al. (2013) with Eq. (12), for NGC 4486 and NGC 5846, respectively. This result supports our spherical approximation and our choice of $R = 4800$ arcsec as the extension of the radial grid that we will adopt in our dynamical model in Sect. 5.1.

3.2. Number density profiles of GCs

The number density profiles of GCs are from Pota et al. (2015) for NGC 1407, from Strader et al. (2011) for NGC 4486, and from Pota et al. (2013) for NGC 5846. Each GC sample is separated into a blue and a red sample according to the colour thresholds listed in Table 1. To ensure the magnitude completeness of the GCs samples in all the three galaxies, Pota et al. (2013) remove the sources fainter than $M_i = -8.0$ in the i -band. This magnitude limit corresponds to the peak of the GC luminosity function that has a roughly Gaussian shape (e.g. Harris et al. 1991; Whitmore et al. 1995; Kundu & Whitmore 1998). Moreover, the samples might be contaminated by ultracompact dwarf galaxies (UCDs), that are a kinematically and spatially distinct population from the GCs. Therefore, Pota et al. (2013) remove the sources brighter than $M_i = -11.6$. This luminosity is 1 mag brighter than ω Cen, the brightest GC in the Milky Way, and brighter objects are likely to be UCDs. NGC 1407, NGC 4486, and NGC 5846 have 379, 737, and 195 confirmed GCs, respectively (Table 1). Imposing the magnitude range $-11.6 < M_i < -8.0$ removes 72 objects from the NGC 1407 sample, and 53 objects from the NGC 4486 sample, whereas the NGC 5846 sample remains unaffected.

In addition to this photometric selection, Pota et al. (2013, 2015) apply a kinematic selection on the two separated populations of blue and red GCs. Despite Galactic stars and GCs are two populations whose velocity distributions are usually well distinct, sometimes the population of stars might have a low-velocity tail so that a Galactic star could erroneously be identified as a GC. Pota et al. (2013, 2015) thus remove the sources whose velocity is more than 3σ discrepant from the mean velocity of the 20 closest neighbours in the GC sample, where σ is the velocity dispersion of these 20 neighbours (Merrett et al. 2003). This kinematic criterion removes 6, 5, and 2 objects from the NGC 1407, NGC 4486, and NGC 5846 samples, respectively. The sizes of the final samples of blue and red GCs for each galaxy are listed in Table 1.

Each GC sample is binned in circular annuli around the galaxy centre. The background-subtracted surface number density profiles, along with their Poissonian uncertainties, are shown in Fig. 1.

Table 2: Parameters of the stellar surface brightness profile of NGC 4486.

L_k [L_\odot] (1)	σ_k [arcsec] (2)
3.26333×10^7	0.31847133
6.31462×10^7	0.85316859
1.42502×10^8	1.9878101
1.20241×10^9	4.3688105
2.92993×10^9	7.0315581
6.16303×10^9	11.941329
1.08416×10^{10}	21.809295
2.11184×10^{10}	48.869046
3.15170×10^{10}	120.71397

Table 3: Parameters of the stellar surface brightness profile of NGC 5846.

L_k [L_\odot] (1)	σ_k [arcsec] (2)
3.09594×10^8	1.3004914
6.31938×10^8	2.0720509
2.52404×10^9	4.7753466
2.41652×10^9	8.9026766
8.05893×10^9	16.353135
9.26616×10^9	32.666416
2.29889×10^{10}	78.813294

3.2.1. NGC 5846

We model the profiles of the blue and red GCs in NGC 5846 with the Sérsic profile

$$N_{\text{GC}}(R) = N_e \exp \left\{ -b_{n_s} \left[\left(\frac{R}{R_e} \right)^{\frac{1}{n_s}} - 1 \right] \right\}, \quad (16)$$

where the parameters R_e , N_e , and n_s have similar meaning of those in Eq. (8).

We estimate the free parameters of the surface number density profiles of the blue and red GCs with a Monte Carlo Markov Chain (MCMC) method with a Metropolis–Hastings acceptance criterion. Details of this algorithm are in Sect. 5.2. We run the MCMC for 2×10^6 steps with 10^5 burn-in elements to achieve the convergence of the chains, according to the Geweke (1992) diagnostics. We adopt flat priors on the free parameters of the model in the ranges listed in Table 4. The upper limit of R_e is the radius of the most external data point of the surface number density; the upper limit of N_e is slightly larger than the surface number density at the smallest R . Therefore, the upper limits of the priors for R_e and N_e are different for the two GC populations. Our posterior distributions are single-peaked. We thus adopt their medians as our parameter estimates and the range between the 15.9 and 84.1 percentiles, which includes 68% of the posterior cumulative distribution, as our parameter uncertainties. These parameters are listed in Table 5. They provide the curves shown in Fig. 1.

3.2.2. NGC 1407 and NGC 4486

We model the surface number densities of the two GC populations in NGC 1407 and NGC 4486 with a Sérsic profile, adopting the parameters obtained by Pota et al. (2015) and Strader et al. (2011) for the two galaxies, respectively. Pota et al. (2015) model

their data with Eq. (16). Strader et al. (2011) adopt the slightly different parametrisation

$$N_{\text{GC}}(R) = N_0 \exp \left[- \left(\frac{R}{R_s} \right)^{\frac{1}{m}} \right]. \quad (17)$$

Table 5 lists the parameters of the models shown in Fig. 1.

For the three galaxies, the 3D number density of the GCs is

$$n_{\text{GC}}(r) = -\frac{1}{\pi} \int_r^{+\infty} \frac{dN_{\text{GC}}}{dR} \frac{dR}{\sqrt{R^2 - r^2}}. \quad (18)$$

3.3. Mass density profiles of the X-ray gas

3.3.1. NGC 1407

For the 3D mass density of the hot X-ray emitting gas, we adopt the model parameters derived by Zhang et al. (2007). They assume spherical symmetry and model the 3D number density profile of the gas, $n_g(r)$, with the two- β function

$$n_g^2(r) = n_{g,1}^2 \left[1 + \left(\frac{r}{R_{c,1}} \right)^2 \right]^{-3\beta_1} + n_{g,2}^2 \left[1 + \left(\frac{r}{R_{c,2}} \right)^2 \right]^{-3\beta_2}. \quad (19)$$

If we assume hydrodynamic equilibrium and an ideal and thermalised gas, $n_g^2(r)$ enters the observed X-ray surface brightness profile

$$S_g(R) = S_0 \int_R^{+\infty} \Lambda(T, Z) n_g^2(r) \frac{r dr}{\sqrt{r^2 - R^2}} + S_{\text{bkg}}, \quad (20)$$

where $T(r)$ and $Z(r)$ are the temperature and the metallicity profiles, $\Lambda(T, Z)$ is the cooling function, and S_{bkg} is the background

Table 4: Priors of the parameters of the GC surface number density models of NGC 5846.

GC sample	N_e [$\frac{\text{GCs}}{\text{arcmin}^2}$]	R_e [arcsec]	n_s
(1)	(2)	(3)	(4)
Blue	$U(0.00, 2.24]$	$U(0.00, 833]$	$U(0.00, 3.00]$
Red	$U(0.00, 2.55]$	$U(0.00, 714]$	$U(0.00, 3.00]$

Notes. U stands for uniform distribution.

Table 5: Parameters of the models of the surface number density of the GCs.

NGC	GC sample	N_e, N_0 [$\frac{\text{GCs}}{\text{arcmin}^2}$]	R_e, R_s [arcsec]	n_s, m	$\chi^2_{\text{red}, \nu}$
(1)	(2)	(3)	(4)	(5)	(6)
1407	Blue	7 ± 1	346 ± 29	1.6 ± 0.2	0.90
	Red	20 ± 2	169 ± 7	1.6 ± 0.2	1.29
4486	Blue	$(6.10 \pm 2.88) \times 10^2$	1 ± 2	3.69 ± 0.47	0.54
	Red	$(5.08 \pm 1.59) \times 10^4$	$(1.6 \pm 1.7) \times 10^{-3}$	5.33 ± 0.24	0.28
5846	Blue	$0.65^{+0.57}_{-0.37}$	324^{+171}_{-100}	$1.39^{+1.02}_{-0.82}$	1.64
	Red	$0.91^{+0.30}_{-0.30}$	268^{+43}_{-35}	$0.95^{+0.87}_{-0.38}$	1.88

Notes. Column 1: galaxy name; Col. 2: colour of the GC population; Cols. 3–5: parameters of the model of the surface number density; Col. 6: reduced chi-square, $\chi^2_{\text{red}, \nu}$, for ν degrees of freedom. The parameters $\{N_e, R_e, n_s\}$, adopted for NGC 1407 and NGC 5846, refer to Eq. (16) and are from Pota et al. (2015) and our MCMC analysis, respectively; the parameters $\{N_0, R_s, m\}$, adopted for NGC 4486, refer to Eq. (17) and are from Strader et al. (2011).

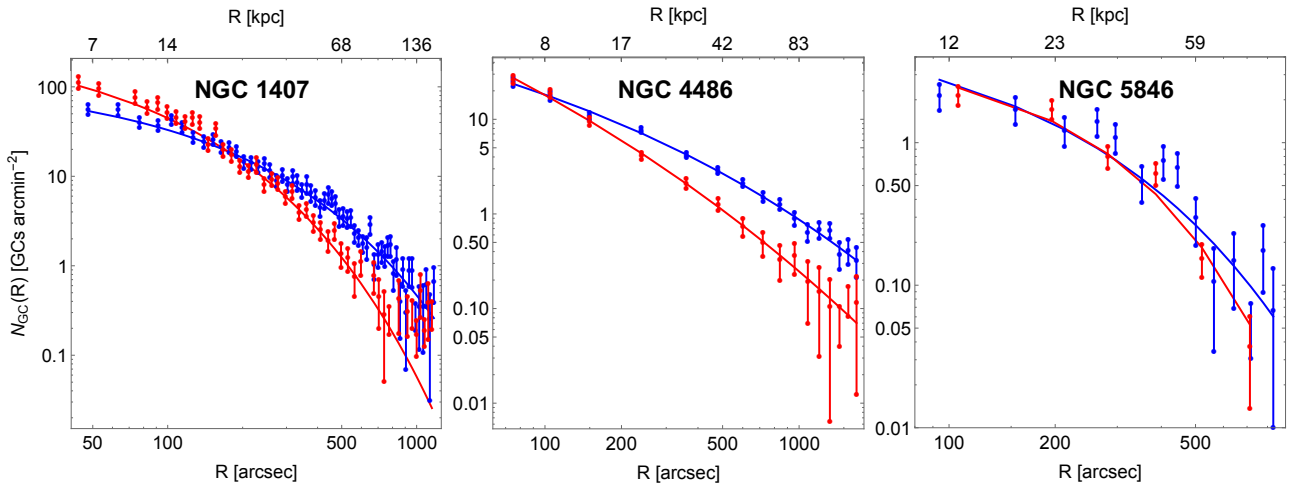


Fig. 1: Surface number density profiles of blue (blue symbols and blue lines) and red (red symbols and red lines) GCs. Blue and red dots with error bars show the measured profiles; the solid lines are the models.

contamination level. The observed $S_g(R)$ was measured with *Chandra* ACIS in the 0.7–7 keV band and with *ROSAT* PSPC in the 0.2–2 keV band. Zhang et al. (2007) fit Eq. (20) to the data and obtain $n_{g,1} = 0.1 \text{ cm}^{-3}$, $n_{g,2} = 3.65 \times 10^{-3} \text{ cm}^{-3}$, $R_{c,1} = (8.42 \pm 0.70) \text{ arcsec}$, $R_{c,2} = (58.3 \pm 0.7) \text{ arcsec}$, $\beta_1 = 0.70 \pm 0.01$, and $\beta_2 = 0.45 \pm 0.01$. They report $n_{g,1}$ and $n_{g,2}$ without uncertainty.

The 3D density profile of the gas entering our model is

$$\rho_g(r) = \mu m_H n_g(r), \quad (21)$$

where $m_H = 1.66054 \times 10^{-27} \text{ kg}$ is the atomic unit mass and $\mu = 0.6$ is the mean molecular weight, which assumes a completely ionised gas and a chemical composition with zero metal-

licity.³ The normalisations $n_{g,1}$ and $n_{g,2}$ yield $\rho_{g,1} = 9.96 \times 10^{-26} \text{ g cm}^{-3}$ and $\rho_{g,2} = 3.64 \times 10^{-27} \text{ g cm}^{-3}$.

3.3.2. NGC 5846

We derive our analytic model of the gas mass density profile from the measurements of Paggi et al. (2017). They use the data from the X-ray observations of the *Chandra* ACIS and *XMM-Newton* MOS instruments. Paggi et al. (2017) model the galaxy as a spherical system and fit the galaxy spectrum of

³ Zhang et al. (2007) assume a non-null metallicity, in the range $[0.21, 1.40] Z_\odot$, where $Z_\odot = 0.0134$ (Asplund et al. 2009). Within this range, μ is basically insensitive to Z . Indeed, adopting $Z = 1.40 Z_\odot$ yields $\mu = 0.5982$.

each concentric circular annulus around the galaxy centre with the Astrophysical Plasma Emission Code (APEC) (Smith et al. 2001). Each circular annulus has a minimum width of 1 arcsec, for *Chandra* data, and of 30 arcsec, for *XMM-MOS* data; this choice yields a finer grid in the innermost galaxy region where most of the *Chandra* data are. The inner and the outer radii of each annulus are chosen to achieve a minimum signal-to-noise $S/N = 100$, for *Chandra* ACIS data, and $S/N = 50$, for *XMM-MOS* data. The spectrum in each circular annulus is the integral of the emission from all the 3D spherical shells along the line of sight. For a source at redshift z and angular diameter distance D_A , the APEC parameters include the temperature of the plasma in each spherical shell, its element abundances, and its normalisation

$$EM = \frac{10^{-14}}{4\pi[(1+z)D_A]^2} \int n_e(r)n_H(r)dV, \quad (22)$$

where the integral is taken over the volume of the 3D spherical shell. The equation above returns EM in cm^{-5} , when D_A is in cm, n_e and n_H in cm^{-3} , and the volume V in cm^3 . In Eq. (22), n_e and n_H are the electron and hydrogen number densities. For a fully ionised gas, $\eta = n_e/n_H = 1.2$. In addition, for NGC 5846, Paggi et al. (2017) assume that n_e and n_H are constant within the shell. Therefore, $4\pi[(1+z)D_A]^2EM = 10^{-14}\eta n_H^2 V$, where V is the volume of the spherical shell. In each spherical shell, the mass density is thus

$$\rho_g = \mu n_H n_H = 10^7 \mu m_H (1+z) D_A \left[\frac{4\pi EM}{\eta V} \right]^{1/2} [\text{g cm}^{-3}], \quad (23)$$

where $\mu = 0.62$ accounts for the metallicity $Z > 0$ of the gas of NGC 5846.⁴

We model the set of data points of the gas mass density in each spherical shell provided by Paggi et al. (2017) with the two- β function in Eq. (19), where the two normalisation constants are now $\rho_{g,1}$ and $\rho_{g,2}$. We estimate the parameters of the gas mass density with the MCMC method described in Sect. 5.2 adopting the Metropolis-Hasting acceptance criterion. Running the chains for 2×10^4 steps with 10^3 burn-in elements is sufficient to reach the convergence of the chains, according to the Geweke (1992) diagnostics. We adopt uniform priors in the intervals listed in Table 6. The upper limits of $R_{c,1}$ and $R_{c,2}$ are the radii of the most external data point of the gas mass density profile in Eq. (23). The upper limits of $\rho_{g,1}$ and $\rho_{g,2}$ are slightly larger than the data point with the smallest R . Our posterior distributions are single-peaked, and we thus adopt the medians of the posterior distributions as our parameter estimates and the range between the 15.9 and 84.1 percentiles as our parameter uncertainties. The parameters of the model, along with their uncertainties, are listed in Table 6.

3.3.3. NGC 4486

We adopt the model derived by Fabricant et al. (1980). They model the X-ray surface brightness profile of the gas, $S_g(R)$, measured in the 0.7–3.0 keV energy band with the *Einstein Observatory*, with

$$S_g(R) = \frac{S_0}{(1 + bR^2 + cR^4 + dR^6)^n}, \quad (24)$$

⁴ In fact, assuming a null metallicity, and thus $\mu = 0.6$, leaves our results unaffected.

where $b = 1.009 \text{ arcmin}^{-2}$, $c = 2.386 \times 10^{-3} \text{ arcmin}^{-4}$, $d = 1.845 \times 10^{-7} \text{ arcmin}^{-6}$, and $n = 0.68$. To obtain the 3D mass density profile, they numerically invert Eq. (24), assuming an isothermal gas. They adopt zero metallicity, with a mean molecular weight $\mu = 0.6$, and model the numerical deprojected density distribution with the function

$$\rho(r) = \frac{\rho_0}{(1 + b'r^2 + c'r^4 + d'r^6)^{n'}}, \quad (25)$$

where $b' = 9.724 \times 10^{-1} \text{ arcmin}^{-2}$, $c' = 3.810 \times 10^{-3} \text{ arcmin}^{-4}$, $d' = 2.753 \times 10^{-8} \text{ arcmin}^{-6}$, $n' = 0.59$, and $\rho_0 = 1.0 \times 10^{-25} \text{ g cm}^{-3}$. These parameters are provided without uncertainty.

3.4. SMBH mass

We include the contribution of the central SMBH in our mass model. We adopt the SMBH masses provided by Rusli et al. (2013): $M_\bullet = 4.5_{-0.4}^{+0.9} \times 10^9 M_\odot$, $6.2_{-0.5}^{+0.4} \times 10^9 M_\odot$, and $1.1_{-0.1}^{+0.1} \times 10^9 M_\odot$ for NGC 1407, NGC 4486, and NGC 5846, respectively. We model the mass density of the SMBH as

$$\rho_\bullet(r) = \frac{M_\bullet}{4\pi r^2} \delta(r) \quad (26)$$

where δ is the Dirac δ function. The cumulative mass profile is thus $M(r) = M_\bullet$.

4. Spectroscopic data

4.1. Stellar velocity dispersion profiles

4.1.1. NGC 1407

For NGC 1407, we use the root-mean-square velocity dispersion profile of the stars measured by Pota et al. (2015). They derive the profile from two different data sets, depending on the radial range. For radii in the range $[0, 30]$ arcsec, they use the long-slit data, along the major axis of the galaxy, from the European Southern Observatory Faint Object Spectrograph and Camera (v.2) (EFOSC2) (Proctor et al. 2009). For radii in the range $[40, 110]$ arcsec, they use the multislit Keck/DEIMOS data (Foster et al. 2016), again along the galaxy major axis. In the overlapping range $[30, 40]$ arcsec, they keep both data sets.

The root-mean-square velocity dispersion profile of the stars at the circularised projected radius R is

$$V_{\text{rms}}(R) = [V_{\text{rot}}^2(R) + \sigma^2(R)]^{1/2}, \quad (27)$$

where $\sigma(R)$ is the stellar velocity dispersion and $V_{\text{rot}}(R) = V(R) - V_{\text{sys}}$ is the major axis stellar rotation velocity in the galaxy frame, properly corrected for the angle between the major rotation axis and the galaxy region considered (see Proctor et al. 2009 for details), with $V(R)$ the observed rotation velocity, and V_{sys} the galaxy systemic velocity due to the Hubble flow.⁵

$V_{\text{rot}}(R)$ and $\sigma(R)$ are estimated from the mean and the standard deviation of the Gaussian distribution that best fits the line-of-sight velocity distribution (LOSVD) of the stars derived from the spectral line profile (Cappellari 2008; Cappellari et al. 2013).

⁵ Pota et al. (2015) and Pota et al. (2013) approximate V_{sys} with the galaxy heliocentric velocity V_{hel} listed in Table 1. V_{hel} actually depends on the date of the observation, but the difference between V_{sys} and V_{hel} is small enough to leave the results for the dynamical model unaffected. We adopt the same approximation throughout the paper.

Table 6: Priors and parameters of the 3D mass density model of the hot X-ray emitting gas of NGC 5846.

$\rho_{g,1}$ [$10^{-26} \frac{\text{g}}{\text{cm}^3}$] (1)	$\rho_{g,2}$ [$10^{-26} \frac{\text{g}}{\text{cm}^3}$] (2)	$R_{c,1}$ [arcsec] (3)	$R_{c,2}$ [arcsec] (4)	β_1 (5)	β_2 (6)
$U(0, 12.6]$	$U(0, 12.6]$	$U(0, 368]$	$U(0, 368]$	$U(0, 3]$	$U(0, 3]$
$3.21^{+0.62}_{-1.21}$	$6.05^{+0.69}_{-0.68}$	34^{+13}_{-9}	18^{+4}_{-5}	$0.4985^{+0.0026}_{-0.0007}$	$0.95^{+0.52}_{-0.47}$

Notes. U stands for uniform distribution.

Cappellari et al. (2006) and Cappellari et al. (2007) use semi-analytic dynamical models to show that $V_{\text{rms}} = (V_{\text{rot}}^2 + \sigma^2)^{1/2}$ obtained from this Gaussian fit is a better estimator of the second moment of the velocity distribution than the second moment estimated with the integral of the LOSVD modelled with a Gauss-Hermite parametrisation (van der Marel & Franx 1993; Gerhard 1993). This result is due to the sensitivity of V_{rot} and σ to the tails of the LOSVD, which are affected by large observational uncertainties (Cappellari 2008; Cappellari et al. 2013).

The analysis of Proctor et al. (2009) confirms that NGC 1407 is a slow rotator, namely $V_{\text{rot}} \ll \sigma$; therefore, Eq. (27) yields $V_{\text{rms}}(R) \approx \sigma(R)$. To obtain the final $V_{\text{rms}}(R)$ profile, Pota et al. (2015) fold and average the data with respect to the galaxy centre.

In our dynamical model described in Sect. 5, we assume an orbital anisotropy parameter β independent of 3D radius r , as Pota et al. (2015) do. However, by fitting Schwarzschild orbit-superposition models to their kinematic data, Thomas et al. (2014) infer a variable $\beta(r)$ within $R = 2$ arcsec of NGC 1407. Therefore, Pota et al. (2015) only consider the V_{rms} profile beyond $R = 2$ arcsec = 0.272 kpc. The top-left panel of Fig. 2 shows the $V_{\text{rms}}(R)$ profile of the stars obtained by Pota et al. (2015).

4.1.2. NGC 4486 and NGC 5846

For NGC 4486 and NGC 5846, we derive $V_{\text{rms}}(R)$ from the ATLAS^{3D} survey (Cappellari et al. 2011). All the data are publicly available on the ATLAS^{3D} website.⁶

The available data provide the two-dimensional map of V and σ of the galaxy on the plane of the sky, where V and σ are the observed rotation velocity and velocity dispersion of the stars. In NGC 4486 and NGC 5846, 99.6% and 97.9% of the data points, respectively, have $V/\sigma \leq 0.2$. Therefore these galaxies, like NGC 1407, are slow rotators, and we have $V_{\text{rms}} \approx \sigma$.

We rotate the galaxy map counter-clockwise in a new Cartesian coordinates $(x'_{\text{rot}}, y'_{\text{rot}})$, such that the photometric major axis of the galaxy is aligned with the east-west direction (Krajnović et al. 2011). We iteratively remove the values of $V_{\text{rms}}(x'_{\text{rot}}, y'_{\text{rot}})$ that deviate more than 3 standard deviations from the mean V_{rms} of the entire map (Cappellari et al. 2013). For NGC 4486 and NGC 5846, the procedure converges after 7 and 6 iterations and removes 155 and 201 data points, respectively. This removal is necessary because some data points could be spurious, because of the presence of Milky Way stars or problematic bins at the edge of the field of view (Cappellari et al. 2013). Finally, we transform the two-dimensional map $V_{\text{rms}}(x'_{\text{rot}}, y'_{\text{rot}})$ into a one-dimensional profile, $V_{\text{rms}}(R)$, by folding and averaging the data with respect to the galaxy centre.

This procedure yields $V_{\text{rms}}(R)$ profiles with 2444 and 1752 data points for NGC 4486 and NGC 5846, respectively. These

profiles are shown in the upper middle and right panels of Fig. 2. These numbers are ~ 2 orders of magnitude larger than the number of data points in the kinematic profiles of the GC populations of the two galaxies (see Sect. 4.2). As confirmed by preliminary tests, with these unbalanced datasets the dynamical models are driven by the $V_{\text{rms}}(R)$ of the stars and are basically insensitive to the GC kinematic profiles. To overcome this problem, we bin the stellar kinematic data. Each bin contains a constant number of data points: $N = 111$ for NGC 4486 and $N = 103$ for NGC 5846. NGC 4486 and NGC 5846 have now 22 and 17 binned data, respectively. These binned data are the medians, both in the V_{rms} and R directions, of the values of the N data points in the bin. The uncertainties are the semi-interval between the 15.9 and the 84.1 percentiles of the distributions, which are nearly symmetric, of the data points in the bin.

In general, massive early-type galaxies, like these two galaxies, show negative orbital anisotropy parameters in their central regions, indicating tangential orbits; on the contrary, in the outer regions, the orbits appear radial (Thomas et al. 2014; Rantala et al. 2019). Numerical simulations show that this difference in the stellar orbits might originate if massive elliptical galaxies form from the merging of two progenitors with mass ratios larger than 1/3 (Rantala et al. 2019): at the centre of the newborn galaxy, the gravitational torques caused by the merging of the SMBHs of the two parent galaxies cause a reversal of the orbit behaviour, from radial to tangential. Therefore, because we assume below an orbital anisotropy parameter β independent of radius r , we exclude the innermost 2 arcsec in the kinematic profiles of NGC 4486 and NGC 5846. This projected radius corresponds to 0.167 kpc and 0.235 kpc for NGC 4486 and NGC 5846, respectively.

4.2. Velocity dispersion profiles of the GCs

4.2.1. NGC 4486 and NGC 5846

We derive the V_{rms} profiles of the GCs in NGC 4486 and NGC 5846 following the procedure of Pota et al. (2013) and Pota et al. (2015). As already specified in Sect. 3.2, our samples of GCs contain 480 blue GCs and 199 red GCs in NGC 4486 and 91 blue GCs and 102 red GCs in NGC 5846.

We bin each GC population into circular annuli centred on the galaxy centre. Each annulus contains the same number of GCs. Specifically, each bin contains $N = 30$ and $N = 25$ GCs for the blue and red populations in NGC 4486 and $N = 26$ GCs for both populations in NGC 5846. These N 's are a trade-off between too poor bins and a too coarse profile. For NGC 4486, we obtain 16 and 8 bins for the blue and the red GCs, respectively. In NGC 5846, we obtain 6 and 7 bins for the blue and the red GCs, respectively. In NGC 5846, some GCs are common to contiguous bins, so that we have a sufficient number of bins despite the small total number of GCs. The radius R of each bin is the median of the radial coordinates of the GCs in the bin. The V_{rms}

⁶ <http://www-astro.physics.ox.ac.uk/atlas3d/>

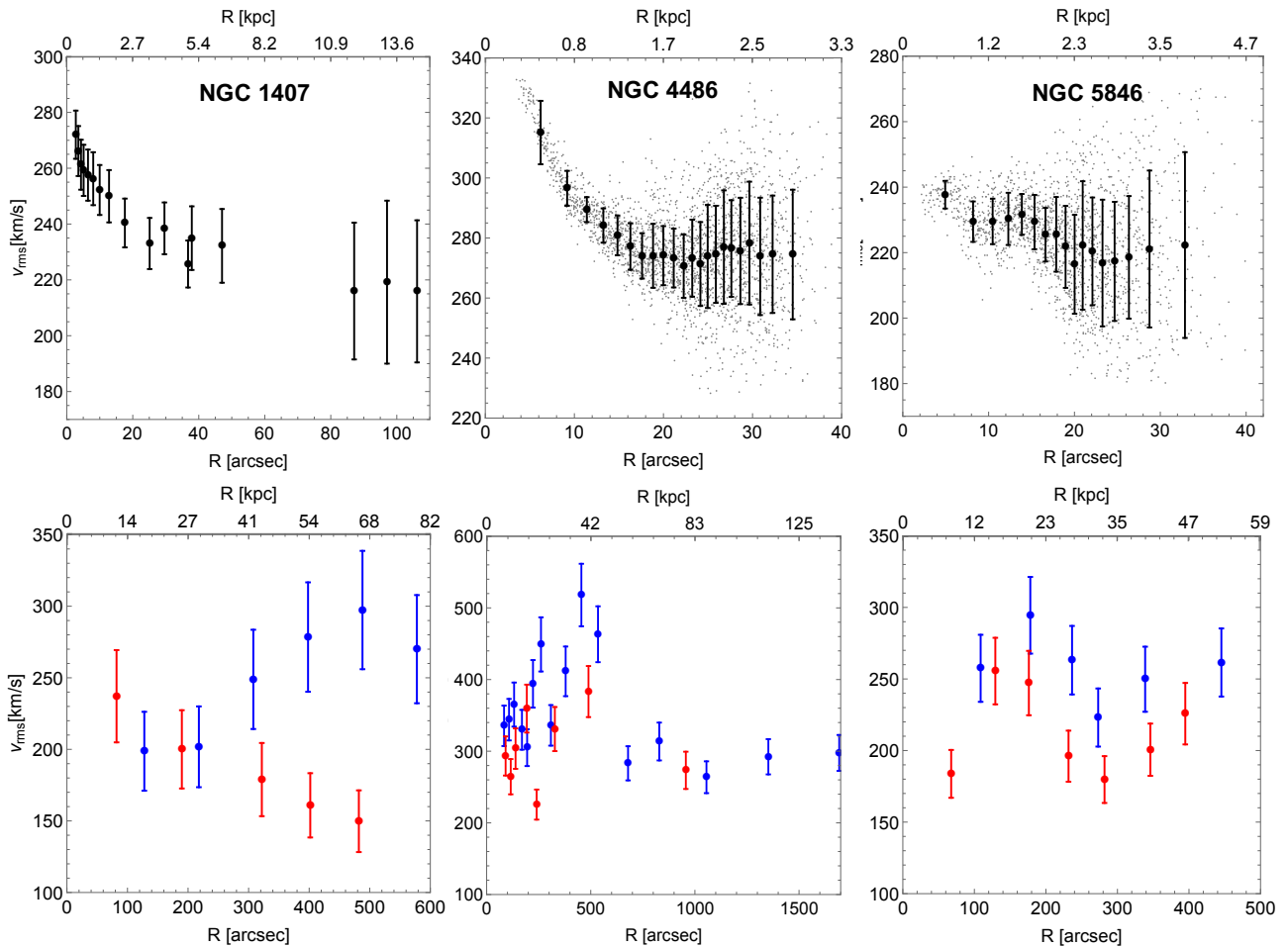


Fig. 2: Root-mean-square velocity dispersion profiles of the stars (upper panels) and of the GCs (lower panels). Each column refers to the galaxy indicated in the upper panels. In the upper middle and right panels, the grey dots and the black dots with error bars show the unbinned and binned profiles, respectively. In the lower panels, the red and blue dots with error bars refer to the blue and red GC populations, respectively. Note the different radial and velocity ranges of the panels.

of the GCs in each bin is (Pota et al. 2013, 2015)

$$V_{\text{rms}}^2 = \frac{1}{N} \sum_{i=1}^N [(V_{\text{rad},i} - V_{\text{sys}})^2 - (\Delta V_{\text{rad},i})^2], \quad (28)$$

where $V_{\text{rad},i}$ is the radial velocity of the i -th GC in the radial bin and $\Delta V_{\text{rad},i}$ is its uncertainty (Jackson 1973; Danese et al. 1980). We take V_{rad} and ΔV_{rad} from Strader et al. (2011), for NGC 4486, and Pota et al. (2013), for NGC 5846. To estimate the errors on each value of V_{rms} we use the procedure reported in Danese et al. (1980), as performed by Pota et al. (2015). For convenience, we report this procedure in Appendix A.

The kinematic profiles of the GCs are shown in Fig. 2. These profiles are ~ 48 and ~ 13 times more extended than the kinematic profiles of the stars for NGC 4486 and NGC 5846, respectively. In NGC 4486, the root-mean-square velocity dispersion profiles of the GC populations show a bell-like shape that peaks at large radii. This feature suggests that the GC kinematics is influenced by the gravitational potential well of the Virgo cluster whose central giant elliptical galaxy is exactly NGC 4486 (Strader et al. 2011). This shape is common to the stellar velocity dispersion profiles of other elliptical galaxies located at the centre of galaxy clusters, like the brightest cluster galaxy of Abell 383 (Geller et al. 2014).

4.2.2. NGC 1407

We extract the $V_{\text{rms}}(R)$ profiles of the two populations of GCs in NGC 1407 from Fig. 5 of Pota et al. (2015). They derive the profiles with the same procedure that we adopt here for NGC 4486 and NGC 5846. Pota et al. (2015) obtain their kinematic data from nine DEIMOS masks in Pota et al. (2013) and an additional DEIMOS mask in Pota et al. (2015). They have a total sample of 379 GCs. After applying the photometric and kinematic selection criteria detailed in Sect. 3.2, Pota et al. (2015) obtain a sample with 153 blue GCs and 148 red GCs. The kinematic profiles of the blue and red GC populations in NGC 1407 are shown in Fig. 2 and are ~ 5 times more extended than the star profile.

5. Dynamical model

5.1. Basic equations

We model the kinematics of the three E0 galaxies by assuming spherical symmetry and no net rotation, as suggested by the observed slow rotation of the galaxies. We model the velocity dispersion profile of each dynamical tracer $t = \{*, R, B\}$, namely

stars, red GCs, and blue GCs, as

$$V_{\text{rms,t}}^2(R) = \frac{2}{I_t(R)} \int_R^{+\infty} K\left(\beta_t, \frac{r}{R}\right) \nu_t(r) \frac{d\phi}{dr} r dr, \quad (29)$$

which is the solution to the spherical Jeans equations (Jeans 1915; Cappellari 2008; Mamon & Łokas 2005; Pota et al. 2015). In Eq. (29), R is the circularised radius projected onto the sky according to Eq. (7), whereas r is the 3D radius; $I_t(R)$ is the surface brightness of the stars or the surface number density of GCs; $\nu_t(r)$ is the 3D luminosity density of the stars or the 3D number density of GCs; $\phi(r)$ is the gravitational potential; and $\beta_t = 1 - \sigma_\theta^2/\sigma_r^2$ is the orbital anisotropy parameter, with σ_θ and σ_r , the velocity dispersions in the tangential and the radial directions, respectively. We assume β_t to be independent of r . K is the kernel

$$K\left(\beta_t, \frac{r}{R}\right) = \frac{1}{2} \left(\frac{r}{R}\right)^{2\beta_t-1} \left[\left(\frac{3}{2} - \beta_t\right) \sqrt{\pi} \frac{\Gamma(\beta_t - \frac{1}{2})}{\Gamma(\beta_t)} + \beta_t B_{\frac{R^2}{r^2}}\left(\beta_t + \frac{1}{2}, \frac{1}{2}\right) - B_{\frac{R^2}{r^2}}\left(\beta_t - \frac{1}{2}, \frac{1}{2}\right) \right], \quad (30)$$

where $\Gamma(z) = \int_0^{+\infty} t^{z-1} e^{-t} dt$ is the Euler Γ function and $B_x(a, b) = \int_0^x t^{a-1} (1-t)^{b-1} dt$ is the incomplete beta function (see Eq. A16 in Mamon & Łokas 2005). By inserting the RG gravitational field, Eq. (3), into Eq. (29), we obtain

$$V_{\text{rms,t}}^2(R) = \frac{2G}{I_t(R)} \int_R^{+\infty} K\left(\beta_t, \frac{r}{R}\right) \nu_t(r) \frac{M(r)}{\epsilon(\rho)} \frac{dr}{r}. \quad (31)$$

In our model, $M(r)$ is the baryonic mass alone, namely

$$M(r) = M_*(r) + M_g(r) + M_\bullet(r) + M_{\text{GC}}(r), \quad (32)$$

where $M_*(r)$, $M_g(r)$, $M_\bullet(r)$, and $M_{\text{GC}}(r)$ are the cumulative mass profiles of the stars, X-ray emitting gas, SMBH, and GCs, respectively. We estimate the mass profile of the stars as

$$M_*(r) = \Upsilon L_*(r), \quad (33)$$

where $L_*(r)$ is the luminosity profile, Eq. (15), and Υ is the stellar mass-to-light ratio that we assume to be independent of r . In our dynamical model, Υ is a free parameter in the ranges predicted by the stellar population synthesis (SPS) models of Humphrey et al. (2006) and Zhang et al. (2007), in the B -band, and Bell et al. (2003) and Zibetti et al. (2009), in the r -band. These ranges depend on the initial mass function. For the B -band, the range is $[4.0, 11.2] M_\odot/L_\odot$ and the lower and upper limits are set by the Kroupa (2001) and Salpeter (1955) initial mass functions, respectively. For the r -band, the range is $[1.7, 5.5] M_\odot/L_\odot$ and the lower and upper limits are set by the Bottema (1993) and Salpeter (1955) initial mass functions, respectively.

The mass profile of the gas, $M_g(r)$, derives from the integration of its density profile. This density profile is indicated in Eq. (19), for NGC 1407 and NGC 5846, and in Eq. (25) for NGC 4486. For each galaxy, the mass of the SMBH, M_\bullet , is the value reported in Sect. 3.4. For the cumulative mass profile of GCs, we adopt

$$M_{\text{GC}}(r) = 4\pi M_{\text{GC}} \int_0^r \nu_{\text{GC}}(r') r'^2 dr', \quad (34)$$

where $\nu_{\text{GC}}(r)$ is the 3D number density of GCs, Eq. (18), and M_{GC} is a constant in the range of $[10^4 - 10^6] M_\odot$, according to the

typical mass function of GCs (Kimmig et al. 2015; Baumgardt 2017).

Figure 3 shows the mass profile of each component. The stars provide the largest contribution to the total mass of each galaxy in most radial range, except in the very centre, where the SMBH dominates, and in the outskirts of NGC 4486 and NGC 5846, where the gas contribution overcomes the star contribution. The contribution of GCs to the total galaxy mass is always smaller than 1% and we thus ignore it hereafter. Therefore, in the velocity dispersion profile of Eq. (31), we also ignore the GC contribution to the density profile

$$\rho(r) = \rho_*(r) + \rho_g(r) + \rho_\bullet(r), \quad (35)$$

which appears as the argument of the permittivity of Eq. (5).

We solve Eq. (31) by adopting two independent linear grids in the R and the r coordinates. Both grids cover the range $[10^{-4}, 4800]$ arcsec, with a step of 4 arcsec.

5.2. The MCMC approach

For each galaxy, the dynamical model has seven free parameters: four parameters, Υ , ϵ_0 , Q and ρ_c , contribute to the gravitational potential well of the galaxy and are common to the three tracers, and three parameters, β_* , β_B and β_R , are specific for each tracer. Note that the contributions of the X-ray emitting gas and the SMBH to the gravitational potential have no free parameters. For convenience, hereafter, we use the parameters $\mathcal{B}_* = -\log_{10}(1 - \beta_*)$, $\mathcal{B}_B = -\log_{10}(1 - \beta_B)$, $\mathcal{B}_R = -\log_{10}(1 - \beta_R)$, and $\mathcal{P}_c = \log_{10}[\rho_c \text{ (g/cm}^3\text{)}]$. Tangential and radial orbits correspond to $\mathcal{B}_t < 0$ and $\mathcal{B}_t > 0$, respectively, where $t = (*, B, R)$.

We explore this seven-dimensional parameter space with a MCMC algorithm, where we adopt a Metropolis-Hastings acceptance criterion: the random variate $\mathbf{x}_{i+1} = (\Upsilon, \epsilon_0, Q, \mathcal{P}_c, \mathcal{B}_*, \mathcal{B}_B, \mathcal{B}_R)$, at step $i + 1$ of the chain, is obtained from the probability density $G(\mathbf{x}_{i+1}|\mathbf{x}_i)$, which depends on the random variate \mathbf{x}_i at the previous step. For $G(\mathbf{x}|\mathbf{x}_i)$, we adopt a multi-variate Gaussian density distribution with mean value \mathbf{x}_i . We choose the standard deviation of this Gaussian distribution according to the priors: when we adopt uniform priors, the standard deviation is 10% of the range of the prior; when we adopt Gaussian priors, the standard deviation is 1/3 of the standard deviation of the prior.

We adopt the likelihood

$$\mathcal{L}(\mathbf{x}) = \exp\left[-\frac{\chi_{\text{red,tot}}^2(\mathbf{x})}{2}\right], \quad (36)$$

where

$$\chi_{\text{red,tot}}^2(\mathbf{x}) = \frac{\chi_*^2(\mathbf{x}) + \chi_B^2(\mathbf{x}) + \chi_R^2(\mathbf{x})}{n_{\text{dof,tot}}}, \quad (37)$$

and

$$\chi_t^2(\mathbf{x}) = \sum_{i=1}^{N_t} \frac{[V_{\text{rms,mod,t}}(R_i, \mathbf{x}) - V_{\text{rms,data,t}}(R_i)]^2}{\Delta V_{\text{rms,data,t}}^2(R_i)}, \quad (38)$$

where $t = (*, B, R)$, N_t is the number of data points of the tracer, $V_{\text{rms,data,t}}$ and $\Delta V_{\text{rms,data,t}}$ are the measured root-mean-square velocity dispersions at the projected distances R_i , and their uncertainties, and $V_{\text{rms,mod,t}}$ is the root-mean-square velocity dispersion model derived from Eq. (31). The total number of degrees of freedom is

$$n_{\text{dof,tot}} = N_* + N_B + N_R - N_{\text{par}}, \quad (39)$$

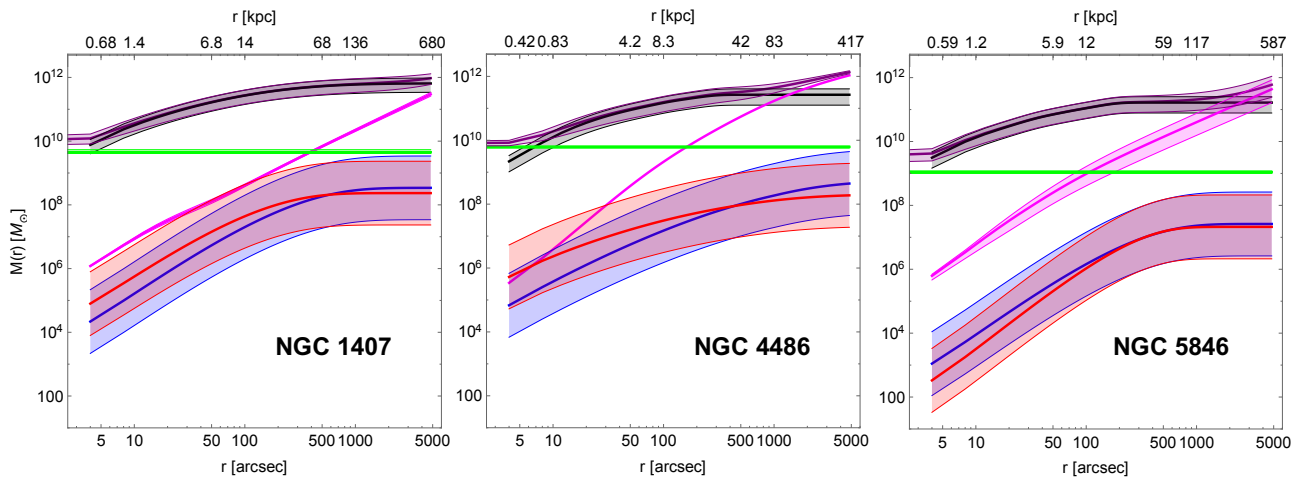


Fig. 3: Cumulative mass profiles of the baryonic components of each galaxy: stars (black solid line), blue GCs (blue solid line), red GCs (red solid line), hot X-ray emitting gas (magenta solid line), and SMBH (green solid line). The purple solid line shows the sum of all the mass contributions. The stellar mass profiles assume $\Upsilon = 7.6 M_{\odot}/L_{\odot}$ for NGC 1407, and $\Upsilon = 3.6 M_{\odot}/L_{\odot}$ for NGC 4486 and NGC 5846. The grey shaded area around the star mass profiles shows the mass variation by adopting mass-to-light ratios in the range $[4.0, 11.2] M_{\odot}/L_{\odot}$, for NGC 1407, and $[1.7, 5.5] M_{\odot}/L_{\odot}$, for NGC 4486 and NGC 5846, in the B - and r -band, respectively. The mass profiles of blue and red GCs assume a GC mass $M_{GC} = 10^5 M_{\odot}$; the blue and red shaded areas show the mass variation by adopting M_{GC} in the range $[10^4, 10^6] M_{\odot}$. The gas mass profile of NGC 4486 has no shaded area because the uncertainties on the adopted mass density profile are unavailable. The green solid lines and shaded areas are the masses of the SMBH and their uncertainties. The purple shaded areas show the possible range of the total baryonic mass profile.

where $N_{\text{par}} = 7$ is the number of the free parameters of the model.

The Metropolis–Hastings ratio is

$$A = \frac{p(\mathbf{x}) \times \mathcal{L}(\mathbf{x}) G(\mathbf{x}|\mathbf{x}_i)}{p(\mathbf{x}_i) \times \mathcal{L}(\mathbf{x}_i) G(\mathbf{x}_i|\mathbf{x})}, \quad (40)$$

where $p(\mathbf{x})$ is the product of the priors of the components of \mathbf{x} . If $A \geq 1$, we accept the proposed combination of free parameters and we thus set $\mathbf{x}_{i+1} = \mathbf{x}$; otherwise, we either set $\mathbf{x}_{i+1} = \mathbf{x}$, with probability A , or $\mathbf{x}_{i+1} = \mathbf{x}_i$, with probability $1 - A$. We adopt 2×10^4 steps for our MCMC, a number sufficient to achieve the chain convergence, according to the Geweke (1992) diagnostics. The first 10^3 elements are discarded as the burn-in chain.

6. Results

6.1. Priors

To model each galaxy with our MCMC analysis, we need to adopt a prior for each of our seven free parameters. For NGC 1407, the photometric information available in the B -band suggests the uniform prior $[4.0, 11.2] M_{\odot}/L_{\odot}$ for Υ . For NGC 4486 and NGC 5846, with photometric information in the r -band, we adopt the uniform prior $[1.7, 5.5] M_{\odot}/L_{\odot}$. We choose both prior ranges according to the ranges expected from the SPS models mentioned in Sect. 5 (Humphrey et al. 2006; Zhang et al. 2007; Bell et al. 2003; Zibetti et al. 2009). For all the three orbital anisotropy parameters, \mathcal{B}_* , \mathcal{B}_B , and \mathcal{B}_R , we adopt the uniform prior $[-1.5, 1.0]$, thus including almost all possible orbits, from very tangential to very radial. Except for the prior of Υ in the r -band for NGC 4486 and NGC 5846, our priors coincide with those adopted by Pota et al. (2015), who model the kinematics of NGC 1407 in Newtonian gravity with a generalised Navarro-Frenk-White dark matter halo (Hernquist 1990; Zhao 1996).

For the three permissivity parameters, we adopt uniform priors in the ranges $(0, 1]$, $[0.01, 2]$, and $[-27, -23]$, for ϵ_0 , Q , and

\mathcal{P}_c , respectively. These priors are those adopted in Cesare et al. (2020), except for ϵ_0 : our range here is wider, compared to the range $[0.1, 1]$ of Cesare et al. (2020).

6.2. Refining the priors

Figures 4–6 show the posterior distributions of the parameters of the model for each galaxy and Fig. 7 shows the models of the V_{rms} profiles whose parameters are the medians of the posterior distributions. The description of the kinematics of NGC 4486 and NGC 5846 shown in Fig. 7 appears satisfactory. However, this result is not shared by NGC 1407, despite the convergence of its MCMC: the model of the blue GCs severely underestimates the corresponding kinematic data. The corner plots in Fig. 4 show that the nearly flat posterior distribution of Q , the broad posterior distributions of ϵ_0 , \mathcal{B}_B , and \mathcal{B}_R without distinct peaks, and the substantial uncorrelation between several pairs of parameters, complicate the identification of the best values of ϵ_0 , Q , \mathcal{B}_B , and \mathcal{B}_R ; therefore, adopting the medians of the posterior distribution for these values is unconvincing.

This conclusion also applies to NGC 4486 and NGC 5846, despite the fact that the estimated parameters appear to provide a proper modelling of their kinematic profiles. Indeed, Figs. 5 and 6 show that the one-dimensional posterior distributions of Q and \mathcal{B}_R of both galaxies are broad and their medians do not coincide with their peaks. In addition, the posterior distributions show that most parameters are independent of each other.

We thus perform a second MCMC analysis with refined prior distributions as follows. For NGC 1407, the first MCMC analysis shows that the values $\epsilon_0 = 0.13$ and $Q = 0.38$ yield a reasonable description of the kinematic data, almost independently of the values of \mathcal{P}_c and of the other parameters. In our second MCMC analysis, for ϵ_0 and Q , we thus adopt Gaussian priors with means and standard deviations $\epsilon_0 = 0.13 \pm 0.05$ and $Q = 0.38 \pm 0.05$. These two means are approximately 1σ smaller than the medians of the posterior distributions of the first MCMC analysis

NGC 1407

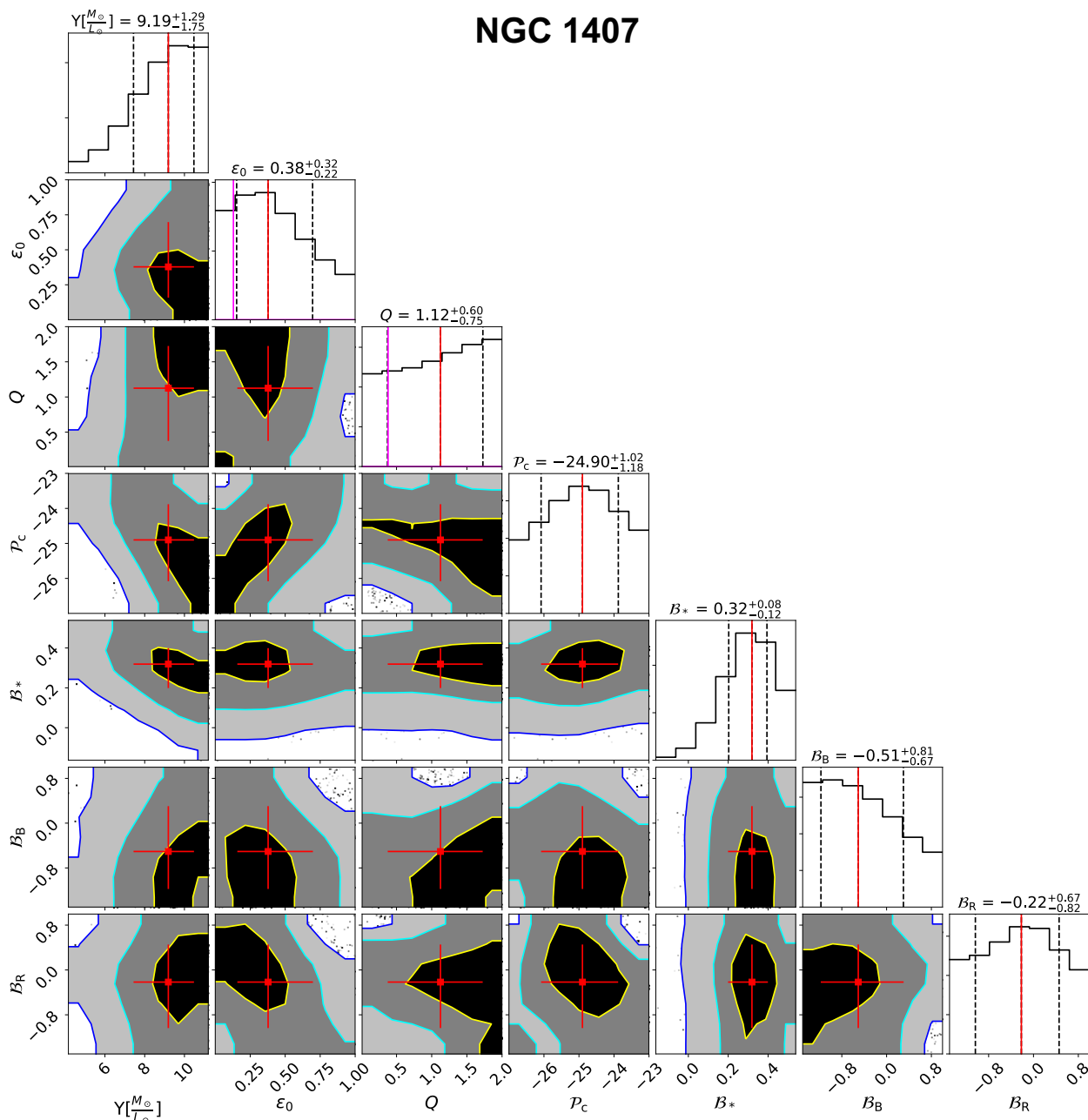


Fig. 4: Posterior distributions of the seven parameters of our first MCMC analysis adopting uniform priors for NGC 1407. The parameters are the stellar mass-to-light ratio, Υ , the anisotropy parameters of the three tracers, B_* , B_B , B_R , and the three permittivity parameters, ϵ_0 , Q , and \mathcal{P}_c . The red squares with error bars show the medians and their uncertainties, set by the 15.9 and 84.1 percentiles of the posterior distributions. The yellow, cyan, and blue contours limit the 1σ , 2σ , and 3σ regions, respectively. The medians and their uncertainties are also reported above each column and in the one-dimensional posterior distributions in the top panels of each column as red solid and black dashed lines, respectively. The magenta solid lines in the one-dimensional posterior distributions of ϵ_0 and Q show the means of the Gaussian priors that we adopt in our second MCMC analysis.

(Fig. 4). For the other parameters, we keep the flat priors of the first analysis.

For NGC 4486 and NGC 5846, the medians of the posterior distributions estimated from the first MCMC analysis reproduce the kinematic data well. We thus simply adopt Gaussian priors peaked on these values for these two galaxies. We set the standard deviations of the Gaussians for all the parameters, except Υ and \mathcal{P}_c , to the mean uncertainties estimated from the first analysis; for Υ and \mathcal{P}_c , we set the standard deviations to three times the mean uncertainties. We adopt larger dispersions for

these two parameters because the relative widths of their posterior distributions derived in the first analysis are in the narrow range [1.6, 22]%; setting the second moment to this range would thus limit the exploration of the parameter space in the second MCMC analysis. On the contrary, the relative widths of the other parameters are in the range [43, 213]% and setting the second moment of the Gaussians to this width provides sufficiently broad priors. The Gaussian priors are set to zero outside the ranges listed in Table 7. This choice prevents the exploration of unphysical or unreasonable values.

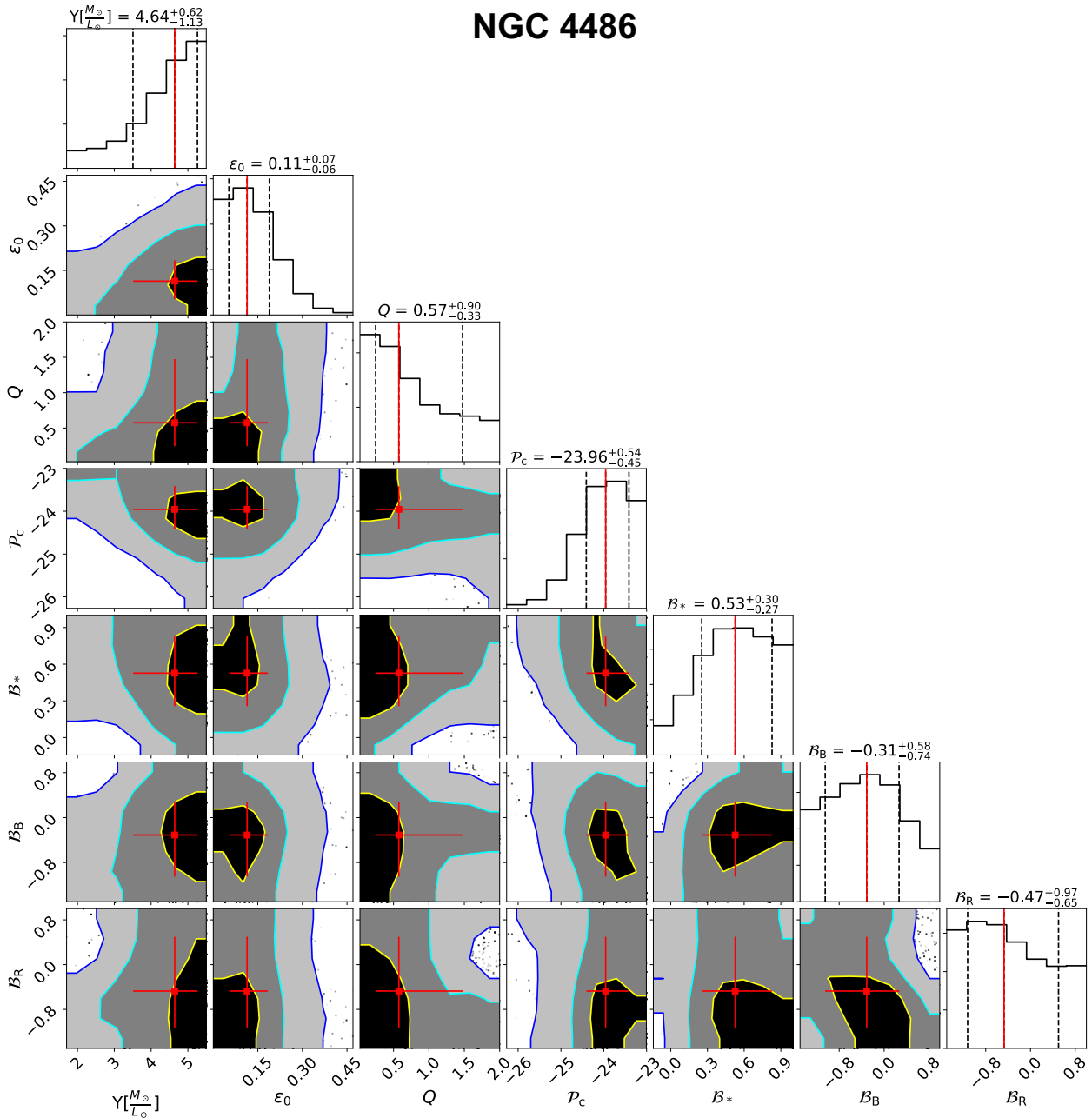


Fig. 5: Same as Fig. 4 for NGC 4486.

6.3. Velocity dispersion profiles

The posterior distributions determined by our second MCMC analysis are shown in Figs. 8–10 and have well-identified peaks. We can thus adopt the medians of these distributions as the parameters of our model. As uncertainties on these parameters, we adopt the range between the 15.9 and the 84.1 percentiles of the posterior distributions. Table 8 lists the parameters that we find and that we use to plot the curves of the models shown in Fig. 11. Table 8 also lists the reduced χ^2 's, Eq. (37), that quantify the agreement between these curves and the data.

The refinement of the priors improves the data description for all the three galaxies. For NGC 1407, the kinematics of the stars, red and blue GCs appear to be satisfactorily described by RG. The underestimation of the profile of the blue GCs disappears. For NGC 4486 and NGC 5846, the kinematic model of

the stars and red GCs also appears appropriate. This result is not shared, however, by the blue GCs. In NGC 5846, RG underestimates the outer points of the measured profile, whereas, in NGC 4486, RG cannot interpolate the peak of the velocity dispersion profile. These data are the main cause of the large values of the χ^2 : if we remove these data points, the reduced χ^2 's decrease from 1.71 to 0.99 and from 3.30 to 2.37, for NGC 5846 and NGC 4486, respectively. These poor fits might originate from the assumption that these two galaxies are isolated rather than embedded in a larger system, as we discuss below. The fits might also partly improve if we remove our assumption that the velocity anisotropy parameters β are independent of radius r or that the galaxies have null net rotation: albeit weak, the net galaxy rotation is not completely absent in the real galaxies.

Nevertheless, RG overall provides a global good description of the kinematic data of the three tracers for all the three galaxies

NGC 5846

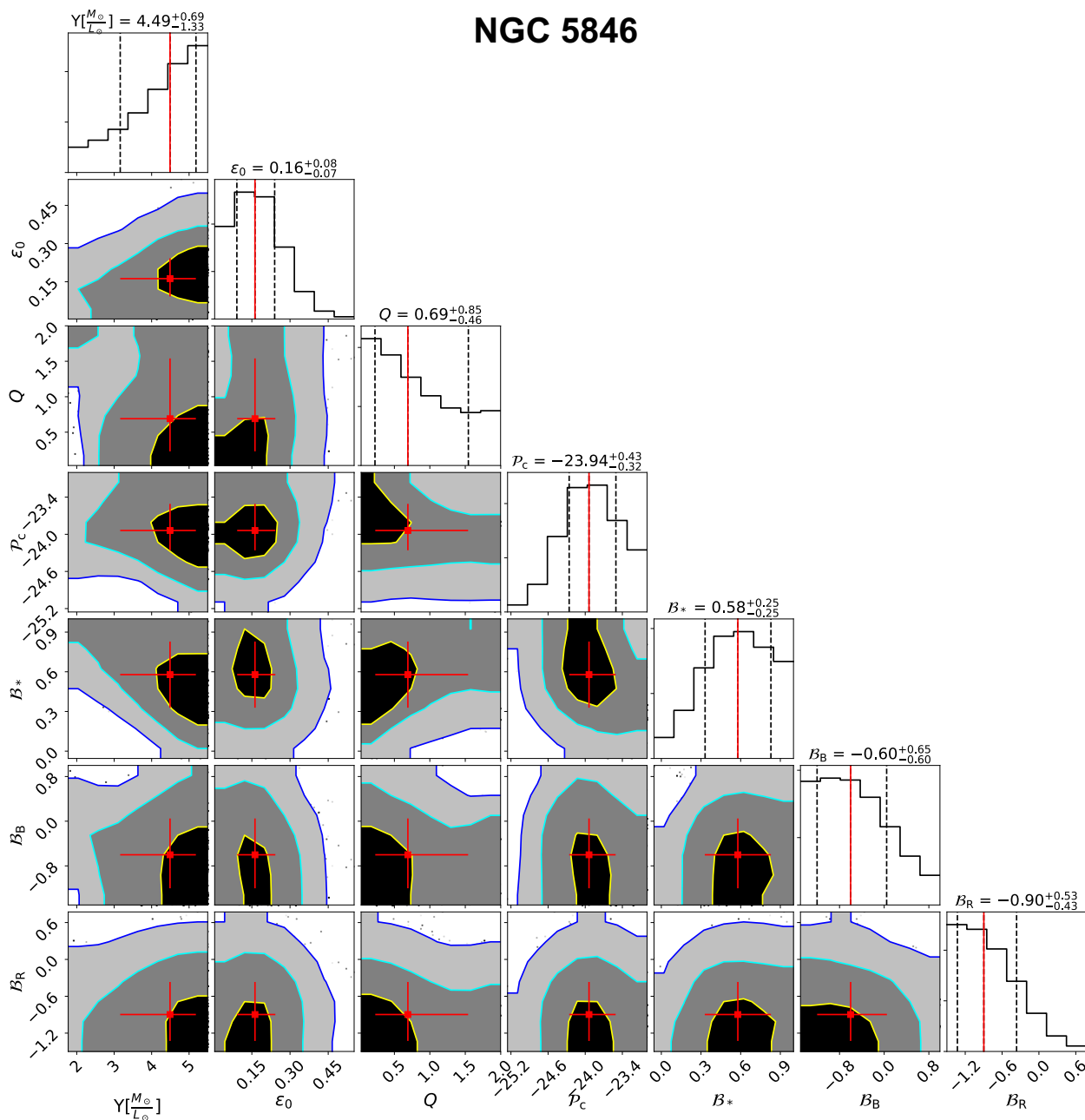


Fig. 6: Same as Fig. 4 for NGC 5846.

with stellar mass-to-light ratios consistent with the SPS models. For NGC 1407, the values of Υ , B_* , B_B , and B_R that we obtain are at $+0.38\sigma$, $+0.67\sigma$, $+0.79\sigma$, and -0.17σ , respectively, from the parameters found by Pota et al. (2015) in their analysis with Newtonian gravity and a dark matter halo.

The RG models require radial orbits for the stars and tangential orbits for the blue GCs in all the three galaxies. The red GCs have tangential orbits in NGC 4486 and NGC 5846, and radial orbits in NGC 1407, in agreement with the result found by Pota et al. (2015) in Newtonian gravity for NGC 1407.

6.4. Parameters of the RG permittivity

The orange squares with error bars in Fig. 12 show the permittivity parameters estimated for the three E0 galaxies: the parameters are consistent with each other within $\sim 1\sigma$, sug-

gesting their universality. Their mean values are $\{\epsilon_0, Q, \mathcal{P}_c\} = \{0.15^{+0.05}_{-0.05}, 0.59^{+0.36}_{-0.25}, -24.51^{+0.58}_{-0.68}\}$. Figure 12 also shows the permittivity parameters derived from 30 disk galaxies of the DMS sample (Cesare et al. 2020): the purple squares with error bars show the means of the parameters estimated for each individual DMS galaxy, whereas the green dots at the centre of the shaded areas show the global values derived with an approximate procedure from the entire 30 galaxy sample.

Our estimates of \mathcal{P}_c and Q are within 1σ from the DMS mean values, whereas the DMS permittivity of the vacuum ϵ_0 is within 2.5σ from our values. This marginal discrepancy might originate from our simplistic modelling of the E0 galaxies. Indeed, here we assume that these galaxies have not net rotation and are relaxed and isolated, whereas, in fact, these galaxies are in clusters or groups and show sign of interactions with nearby galaxies: NGC 1407 is at the centre of the Eridanus A group (Brough

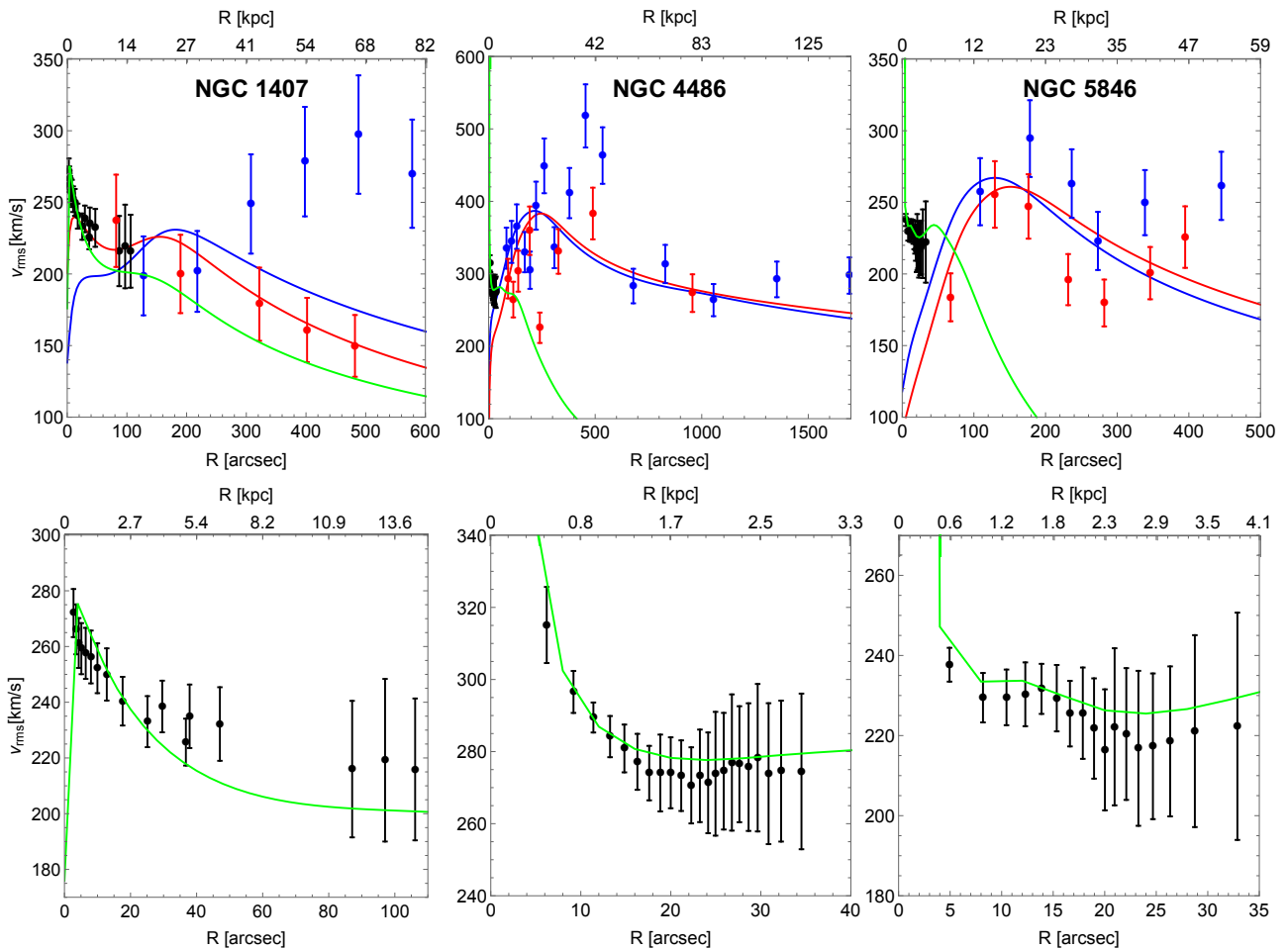


Fig. 7: Models of the root-mean-square velocity dispersion profiles emerging from our first MCMC analysis. In the upper panels, the green, blue, and red solid lines show the model profiles for the stars, blue GCs, and red GCs, respectively. The lower panels show a zoom-in of the stellar profiles. The dots with error bars are the measured profiles from Fig. 2.

et al. 2006) and certainly feels the gravitational influence of its neighbour galaxy NGC 1400. NGC 4486, namely M87, is the central giant elliptical galaxy of the Virgo cluster (Strader et al. 2011) and NGC 5846 is the central and brightest galaxy of a galaxy group (Mahdavi et al. 2005). Moreover, the GC sample of NGC 5846 might be contaminated by the GCs of its neighbour NGC 5846A (Pota et al. 2013). The environment has a relevant effect on the intensity of the gravitational field in RG (Matsakos & Diaferio 2016); this effect clearly propagates into the actual values of the permittivity parameters. The environmental effects can also be responsible for the poor fitting of the velocity dispersion profiles of the blue GCs of NGC 4486 and NGC 5846 shown in Fig. 11. It would thus be necessary to refine our model by taking into account the effects of both rotation and the mass distribution surrounding the galaxies.

The tension between our permittivity parameters and those derived from the DMS sample might become more severe if we consider the DMS global values, namely the green dots in Fig. 12. Our \mathcal{P}_c and Q are still within 3σ from the DMS parameters, whereas ϵ_0 shows a $\sim 10\sigma$ tension, clearly driven by the small width of the posterior distribution of the DMS global value. This discrepancy might be due to the approximate procedure adopted by Cesare et al. (2020) to estimate this DMS global value: with their MCMC analysis, Cesare et al. (2020) only explore the space of the three permittivity parameters while keeping fixed the mass-to-light ratio Υ and the disk-scale height h_z

of each of the 30 individual galaxies. This approach is a shortcut to the appropriate, but computationally overwhelming, procedure of exploring the 63-dimensional parameter space of the full sample, namely the properties, Υ and h_z , of all the galaxies and the three permittivity parameters. The set of the permittivity global parameters returned by this shortcut still describes the kinematic profiles of each galaxy, but the agreement is poorer than the agreement obtained by modelling each galaxy individually. Therefore these values of the permittivity parameters should be considered with caution.

7. Discussion and conclusion

We use the kinematic information of the GCs in the outer regions of three E0 galaxies from the SLUGGS survey (Pota et al. 2013; Brodie et al. 2014; Forbes et al. 2017) to show that RG can describe the kinematics of spherical systems without requiring the existence of dark matter. Our results complement the ability of RG to describe the rotation curves and the vertical velocity dispersion profiles of 30 disk galaxies from the DMS survey (Bershady et al. 2010) shown in Cesare et al. (2020). In RG, the dark matter is mimicked by the gravitational permittivity, a monotonic function of the local mass density that is expected to be universal. For the permittivity, according to Matsakos & Diaferio (2016) and Cesare et al. (2020), we adopt a smooth function

Table 7: Priors of the parameters of the kinematic model, Eq. (31), adopted in our final analysis.

NGC	Υ $\left[\frac{M_\odot}{L_\odot}\right]$	ϵ_0	Q	\mathcal{P}_c	\mathcal{B}_*	\mathcal{B}_B	\mathcal{B}_R
(1)	(2)	(3)	(4)	(5)	(6)	(7)	(8)
1407	$U[4.0, 11.2]$	$G(0.13, 0.05)$ $\in (0, 1]$	$G(0.38, 0.05)$ $\in [0.01, 2]$	$U[-27, -23]$	$U[-1.5, 1.0]$	$U[-1.5, 1.0]$	$U[-1.5, 1.0]$
4486	$G(4.64, 2.64)$ $\in (0, +\infty)$	$G(0.11, 0.07)$ $\in (0, 1]$	$G(0.57, 0.62)$ $\in [0.01, 2]$	$G(-23.96, 1.50)$ $\in [-27, -23]$	$G(0.53, 0.29)$ $\in [-1.5, 1.0]$	$G(-0.31, 0.66)$ $\in [-1.5, 1.0]$	$G(-0.47, 0.81)$ $\in [-1.5, 1.0]$
5846	$G(4.49, 3.03)$ $\in (0, +\infty)$	$G(0.16, 0.08)$ $\in (0, 1]$	$G(0.69, 0.66)$ $\in [0.01, 2]$	$G(-23.94, 1.14)$ $\in [-27, -23]$	$G(0.58, 0.25)$ $\in [-1.5, 1.0]$	$G(-0.60, 0.63)$ $\in [-1.5, 1.0]$	$G(-0.90, 0.48)$ $\in [-1.5, 1.0]$

Notes. Column 1: galaxy name; Cols. 2–8: free parameters of the kinematic model, Eq. (31). U and G stand for uniform and Gaussian distributions, respectively. For the uniform distributions, we list the entire range. For the Gaussian distributions, we list the mean, the standard deviation and, on the second line of each galaxy, the range explored by the MCMC.

Table 8: Parameters estimated from the three dynamical tracers.

NGC	Υ $\left[\frac{M_\odot}{L_\odot}\right]$	ϵ_0	Q	\mathcal{P}_c	\mathcal{B}_*	\mathcal{B}_B	\mathcal{B}_R	$\chi^2_{\text{red,tot}}$
(1)	(2)	(3)	(4)	(5)	(6)	(7)	(8)	(9)
1407	$8.4^{+1.6}_{-2.1}$	$0.14^{+0.05}_{-0.05}$	$0.37^{+0.06}_{-0.05}$	$-25.13^{+0.77}_{-0.81}$	$0.35^{+0.08}_{-0.10}$	$-0.58^{+0.80}_{-0.58}$	$0.17^{+0.56}_{-0.83}$	1.03
4486	$5.6^{+1.2}_{-1.6}$	$0.12^{+0.04}_{-0.04}$	$0.64^{+0.48}_{-0.30}$	$-24.33^{+0.56}_{-0.77}$	$0.45^{+0.25}_{-0.22}$	$-0.20^{+0.45}_{-0.52}$	$-0.42^{+0.87}_{-0.77}$	3.30
5846	$5.1^{+1.5}_{-1.5}$	$0.18^{+0.05}_{-0.05}$	$0.75^{+0.53}_{-0.39}$	$-24.08^{+0.42}_{-0.45}$	$0.51^{+0.21}_{-0.19}$	$-0.68^{+0.50}_{-0.58}$	$-0.92^{+0.37}_{-0.45}$	1.71

Notes. Column 1: galaxy name; Cols. 2–8: medians of the posterior distributions with their uncertainties; Col. 9: reduced chi-square, $\chi^2_{\text{red,tot}}$, from Eq. (37).

that depends on three parameters: the permittivity of the vacuum ϵ_0 , the critical density ρ_c , and the transition slope Q .

We find that the sets of parameters of the three E0 galaxies are consistent with each other within $\sim 1\sigma$. Their values averaged over the three galaxies are $\{\epsilon_0, Q, \log_{10}[\rho_c \text{ (g/cm}^3\text{)}]\} = \{0.15^{+0.05}_{-0.05}, 0.59^{+0.36}_{-0.25}, -24.51^{+0.58}_{-0.68}\}$. With this permittivity, RG requires stellar mass-to-light ratios in agreement with SPS models and tangential or radial orbits for the GCs, depending on the galaxy and the colour of the GCs. In particular, for NGC 1407, the mass-to-light ratio and the orbital anisotropy parameters are within 1σ from the values found by Pota et al. (2015), who model this galaxy with Newtonian gravity and a dark matter halo.

By modelling the kinematic properties of each individual DMS disk galaxy, Cesare et al. (2020) derive the mean values of the permittivity parameters $\{\epsilon_0, Q, \log_{10}[\rho_c \text{ (g/cm}^3\text{)}]\} = \{0.56 \pm 0.16, 0.92 \pm 0.71, -25.30 \pm 1.22\}$. The mean values of Q and $\log_{10}\rho_c$ are within 1σ from the parameters we find here, whereas ϵ_0 is within 2.5σ . These combined results thus support the universality of the parameters of the RG permittivity.

Cesare et al. (2020) also derive a set of global parameters $\{\epsilon_0, Q, \log_{10}[\rho_c \text{ (g/cm}^3\text{)}]\} = \{0.661^{+0.007}_{-0.007}, 1.79^{+0.14}_{-0.26}, -24.54^{+0.08}_{-0.07}\}$ with a MCMC analysis where the mass-to-light ratio and the disk thickness of each individual galaxy are kept fixed. This simplified approach returns an approximate estimate of the unique set of the permittivity parameters capable of describing the entire sample of the 30 DMS disk galaxies. This analysis of Cesare et al. (2020) is suggestive of the possible universality of the permittivity parameters, but their actual values should be taken with caution. The global DMS values of $\log_{10}\rho_c$ and Q found by Cesare et al. (2020) are within 3σ from the values we find here and are thus still consistent with the expected universality, whereas

the global DMS ϵ_0 is $\sim 10\sigma$ discrepant. This discrepancy is mostly driven by the width of the posterior distribution found by Cesare et al. (2020) which is small when compared to the uncertainties of the corresponding mean values (Fig. 12). If this width is not severely underestimated, this discrepancy might highlight at least three different possible problems: a simplistic model of the ellipticals, an incorrect form of the permittivity, or a fundamental fault of RG.

The model of the ellipticals that we adopt here is oversimplified, because we treat them as isolated systems and completely neglect the galaxy net rotation. Indeed, NGC 1407 and NGC 5846 are within galaxy groups and NGC 4486 is the central galaxy of the Virgo cluster. Neglecting the galaxy environment can clearly overlook relevant interactions with neighbour galaxies that could actually affect the parameters of the permittivity. Including these environmental effects requires modelling all the galaxies within the system at the same time, with each galaxy modelled according to its morphological type and shape. Properly modelling such a system is arduous and its non-linear effects are difficult to assess at the present stage. We cannot thus exclude that they might be part, if not all, of the cause of the possible tension on ϵ_0 that we find here. Alternatively, the explicit form of the permittivity $\epsilon(\rho)$ (Eq. (5)), that is chosen arbitrarily, might actually be inappropriate, especially in the low-density regime: hints from the weak-field limit of the covariant version of RG (Sanna et al., in preparation) might suggest a better motivated permittivity that might alleviate the tension. Finally, all of the above might turn out to play a negligible role, and this possible tension on the permittivity of the vacuum might simply betray a fundamental fault of RG.

Acknowledgements. We sincerely thank Xavier Hernández and Federico Lelli for their precious advice and detailed comments that improved the presentation of this work, and Alessandro Paggi and Valentina Missaglia, for their help in the modelling of the gas of NGC 5846 and of the number density profiles of

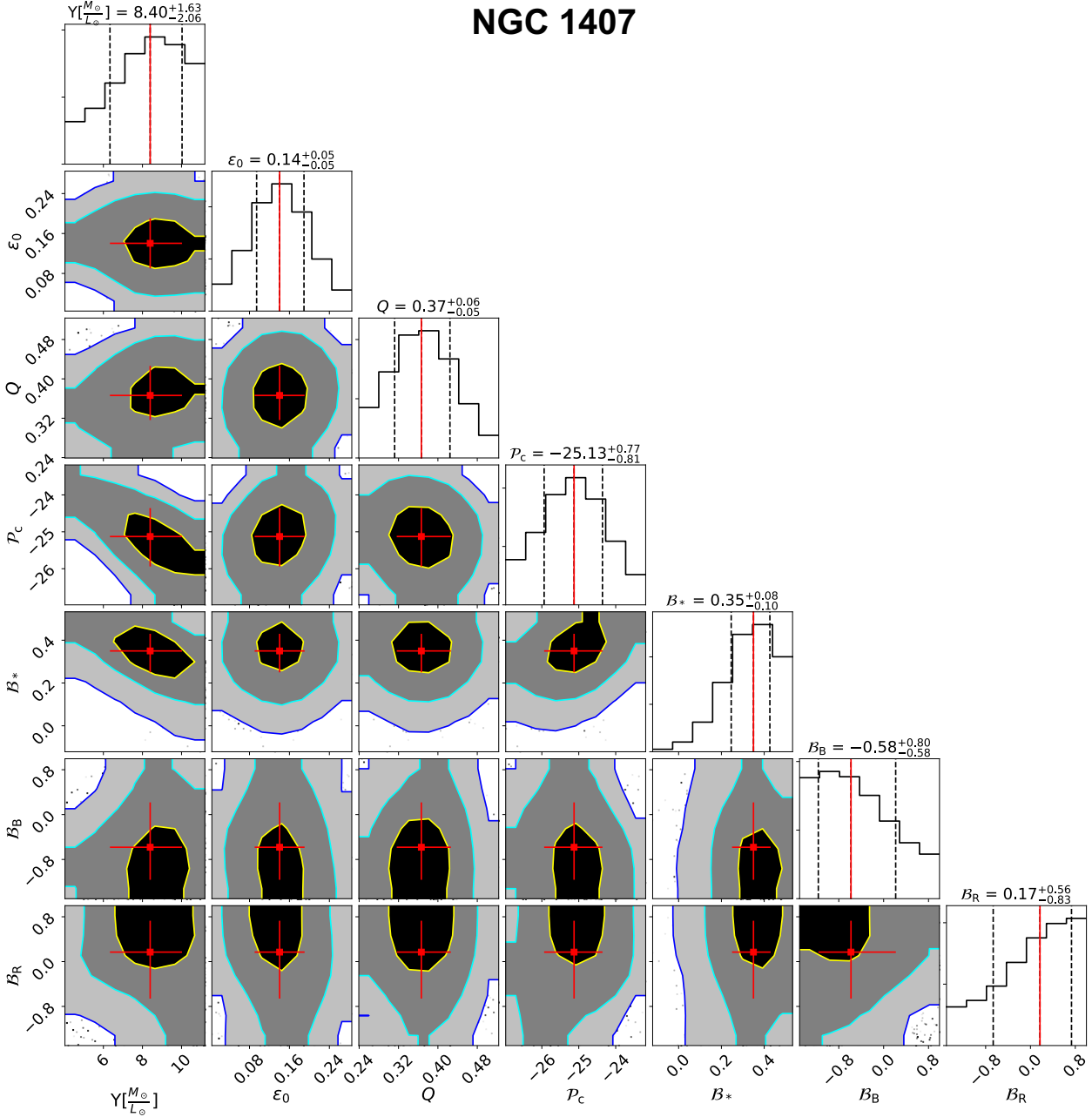


Fig. 8: Same as Fig. 4 for our second MCMC analysis.

the GCs. We also thank Michele Cappellari, for his help in the derivation of the stellar root-mean-square velocity dispersion profiles of NGC 4486 and NGC 5846. We thank Compagnia di San Paolo (CSP) for funding the graduate-student fellowship of VC. We also acknowledge partial support from the INFN grant InDark and the Italian Ministry of Education, University and Research (MIUR) under the *Departments of Excellence* grant L.232/2016. This research has made use of NASA's Astrophysics Data System Bibliographic Services.

References

- Abazajian, K. N., Adelman-McCarthy, J. K., Agüeros, M. A., et al. 2009, *ApJS*, 182, 543
- Ashman, K. M. & Zepf, S. E. 1998, *Cambridge Astrophysics Series*, 30
- Asplund, M., Grevesse, N., Sauval, A. J., & Scott, P. 2009, *ARA&A*, 47, 481
- Azevedo, R. P. L. & Avelino, P. P. 2018, *Phys. Rev. D*, 98, 064045
- Bassino, L. P., Richtler, T., & Dirsch, B. 2006, *MNRAS*, 367, 156
- Baumgardt, H. 2017, *MNRAS*, 464, 2174
- Bell, E. F., McIntosh, D. H., Katz, N., & Weinberg, M. D. 2003, *ApJS*, 149, 289
- Bershady, M. A., Verheijen, M. A. W., Swaters, R. A., et al. 2010, *ApJ*, 716, 198
- Bertacca, D., Bartolo, N., & Matarrese, S. 2010, *Advances in Astronomy*, 2010, 904379
- Bottema, R. 1993, *A&A*, 275, 16
- Brodie, J. P., Romanowsky, A. J., Strader, J., et al. 2014, *ApJ*, 796, 52
- Brodie, J. P. & Strader, J. 2006, *ARA&A*, 44, 193
- Brough, S., Forbes, D. A., Kilborn, V. A., Couch, W., & Colless, M. 2006, *MNRAS*, 369, 1351
- Campigotto, M. C., Diaferio, A., & Fatibene, L. 2019, *Classical and Quantum Gravity*, 36, 245014
- Cappellari, M. 2008, *MNRAS*, 390, 71
- Cappellari, M., Bacon, R., Bureau, M., et al. 2006, *MNRAS*, 366, 1126
- Cappellari, M., Emsellem, E., Bacon, R., et al. 2007, *MNRAS*, 379, 418
- Cappellari, M., Emsellem, E., Krajnović, D., et al. 2011, *MNRAS*, 413, 813
- Cappellari, M., Scott, N., Alatalo, K., et al. 2013, *MNRAS*, 432, 1709
- Carneiro, S. 2018, *General Relativity and Gravitation*, 50, 114
- Cesare, V., Diaferio, A., Matsakos, T., & Angus, G. 2020, *A&A*, 637, A70
- Ciotti, L. & Bertin, G. 1999, *A&A*, 352, 447
- Cyburtt, R. H., Fields, B. D., Olive, K. A., & Yeh, T.-H. 2016, *Reviews of Modern Physics*, 88, 015004

NGC 4486

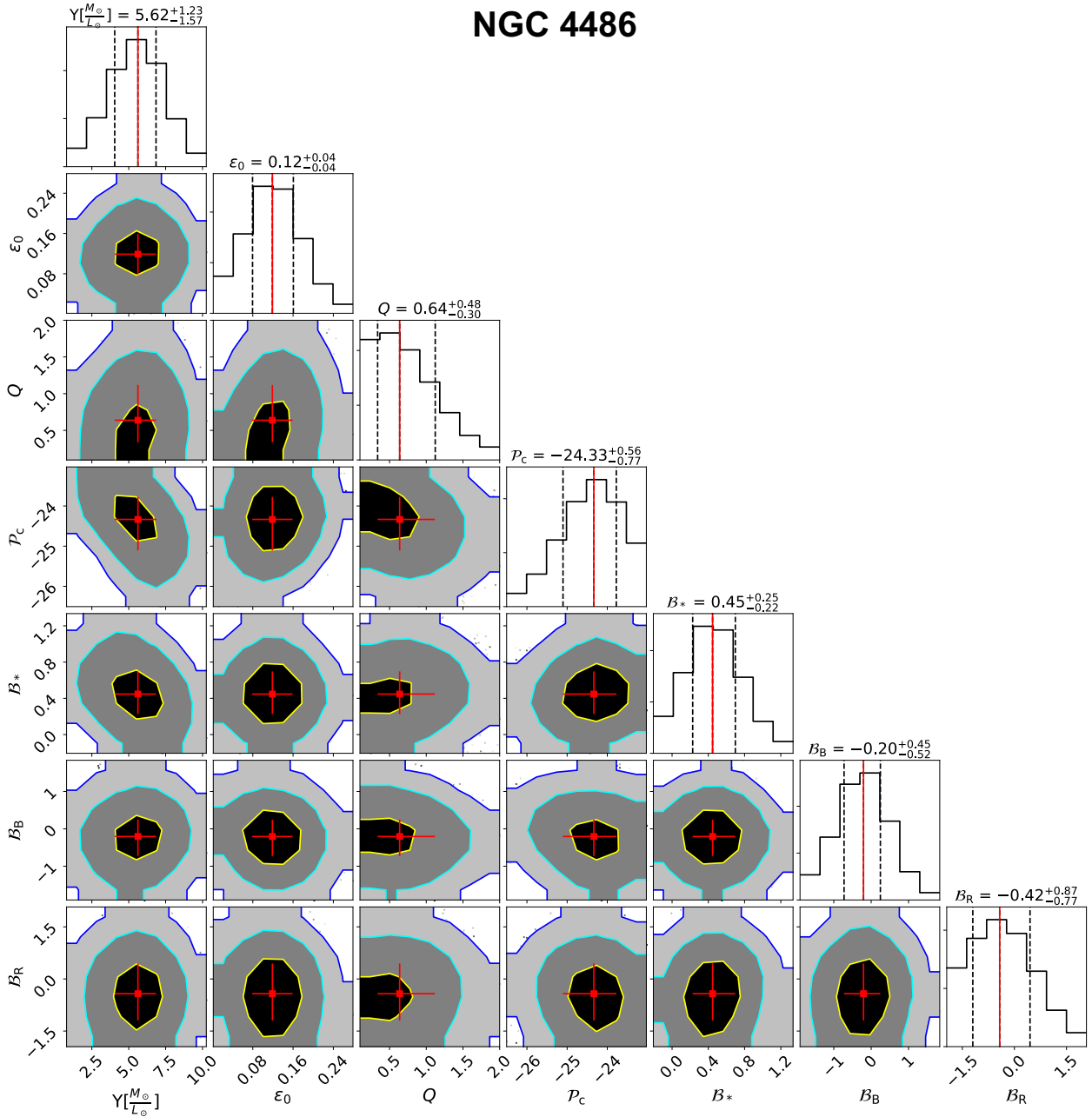


Fig. 9: Same as Fig. 5 for our second MCMC analysis.

Danese, L., de Zotti, G., & di Tullio, G. 1980, *A&A*, 82, 322
Danziger, I. J. 1997, in *Astronomical Society of the Pacific Conference Series*, Vol. 117, *Dark and Visible Matter in Galaxies and Cosmological Implications*, ed. M. Persic & P. Salucci, 28
de Martino, I., Chakrabarty, S. S., Cesare, V., et al. 2020, *Universe*, 6, 107
Dekel, A., Stoehr, F., Mamon, G. A., et al. 2005, *Nature*, 437, 707
Del Popolo, A. 2014, *International Journal of Modern Physics D*, 23, 1430005
Del Popolo, A. & Le Delliou, M. 2017, *Galaxies*, 5, 17
Deur, A. 2014, *MNRAS*, 438, 1535
Deur, A. 2020, arXiv e-prints, arXiv:2010.06692
Diaferio, A. & Ostorero, L. 2009, *MNRAS*, 393, 215
Dodelson, S., Narayanan, V. K., Tegmark, M., et al. 2002, *ApJ*, 572, 140
Durazo, R., Hernandez, X., Cervantes Sodi, B., & Sánchez, S. F. 2017, *ApJ*, 837, 179
Durazo, R., Hernandez, X., Cervantes Sodi, B., & Sanchez, S. F. 2018, *ApJ*, 863, 107
Elizondo, D. & Yepes, G. 1994, *ApJ*, 428, 17
Emsellem, E., Monnet, G., & Bacon, R. 1994, *A&A*, 285, 723
Fabricant, D., Lecar, M., & Gorenstein, P. 1980, *ApJ*, 241, 552
Faifer, F. R., Forte, J. C., Norris, M. A., et al. 2011, *MNRAS*, 416, 155

Famaey, B. & McGaugh, S. S. 2012, *Living Reviews in Relativity*, 15, 10
Ferreira, E. G. M., Franzmann, G., Khoury, J., & Brandenberger, R. 2019, *J. Cosmology Astropart. Phys.*, 2019, 027
Forbes, D. A., Alabi, A., Brodie, J. P., et al. 2017, *AJ*, 153, 114
Forbes, D. A., Ponman, T., & O’Sullivan, E. 2012, *MNRAS*, 425, 66
Foster, C., Pastorello, N., Roediger, J., et al. 2016, *MNRAS*, 457, 147
Geisler, D., Lee, M. G., & Kim, E. 1996, *AJ*, 111, 1529
Geller, M. J., Hwang, H. S., Diaferio, A., et al. 2014, *ApJ*, 783, 52
Gerhard, O. E. 1993, *MNRAS*, 265, 213
Geweke, J. 1992, in *IN BAYESIAN STATISTICS* (University Press), 169–193
Harris, W. E., Allwright, J. W. B., Pritchett, C. J., & van den Bergh, S. 1991, *ApJS*, 76, 115
Hernandez, X. & Jiménez, M. A. 2012, *ApJ*, 750, 9
Hernandez, X., Jiménez, M. A., & Allen, C. 2013a, *MNRAS*, 428, 3196
Hernandez, X., Jiménez, M. A., & Allen, C. 2013b, *ApJ*, 770, 83
Hernandez, X. & Lara-D I. A. J. 2020, *MNRAS*, 491, 272
Hernandez, X., Sussman, R. A., & Nasser, L. 2019, *MNRAS*, 483, 147
Hernquist, L. 1990, *ApJ*, 356, 359
Horne, K. 2006, *MNRAS*, 369, 1667
Hui, L., Ostriker, J. P., Tremaine, S., & Witten, E. 2017, *Phys. Rev. D*, 95, 043541

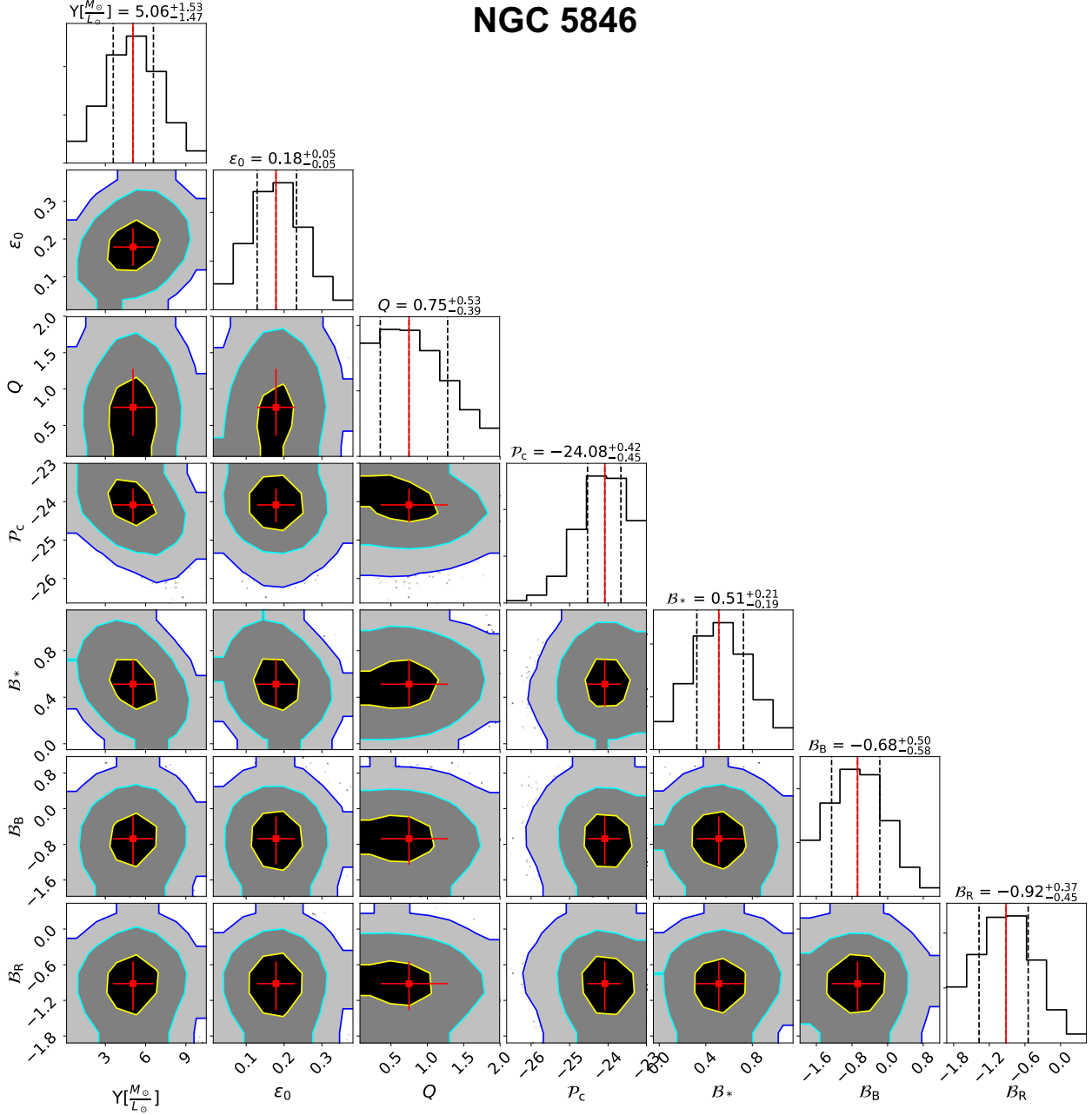


Fig. 10: Same as Fig. 6 for our second MCMC analysis.

Humphrey, P. J., Buote, D. A., Gastaldello, F., et al. 2006, *ApJ*, 646, 899
Jackson, J. C. 1973, *The Observatory*, 93, 19
Jeans, J. H. 1915, *MNRAS*, 76, 70
Jiménez, M. A., García, G., Hernandez, X., & Nasser, L. 2013, *ApJ*, 768, 142
Kimmig, B., Seth, A., Ivans, I. I., et al. 2015, *AJ*, 149, 53
Krajnović, D., Emsellem, E., Cappellari, M., et al. 2011, *MNRAS*, 414, 2923
Kroupa, P. 2001, *MNRAS*, 322, 231
Kroupa, P. 2012, *PASA*, 29, 395
Kundu, A. & Whitmore, B. C. 1998, *AJ*, 116, 2841
Lee, M. G., Park, H. S., Kim, E., et al. 2008, *ApJ*, 682, 135
Mahdavi, A., Trentham, N., & Tully, R. B. 2005, *AJ*, 130, 1502
Mamon, G. A. & Lokas, E. L. 2005, *MNRAS*, 363, 705
Mannheim, P. D. 2019, *International Journal of Modern Physics D*, 28, 1944022
Marsh, D. J. E. 2016, *Phys. Rep.*, 643, 1
Mathews, G., Kedia, A., Sasankan, N., et al. 2020, *JPS Conf. Proc.*, 31, 011033
Mathews, W. G. & Brighenti, F. 2003, *ARA&A*, 41, 191
Matsakos, T. & Diaferio, A. 2016, arXiv e-prints, arXiv:1603.04943
McGaugh, S. 2020, *Galaxies*, 8, 35
Merrett, H. R., Kuijken, K., Merrifield, M. R., et al. 2003, *MNRAS*, 346, L62
Milgrom, M. 2015, *Canadian Journal of Physics*, 93, 107

Napolitano, N. R., Romanowsky, A. J., Coccato, L., et al. 2009, *MNRAS*, 393, 329
Nojiri, S. & Odintsov, S. D. 2011, *Phys. Rep.*, 505, 59
Paggi, A., Kim, D.-W., Anderson, C., et al. 2017, *ApJ*, 844, 5
Planck Collaboration, Aghanim, N., Akrami, Y., et al. 2020, *A&A*, 641, A5
Pota, V., Forbes, D. A., Romanowsky, A. J., et al. 2013, *MNRAS*, 428, 389
Pota, V., Romanowsky, A. J., Brodie, J. P., et al. 2015, *MNRAS*, 450, 3345
Proctor, R. N., Forbes, D. A., Romanowsky, A. J., et al. 2009, *MNRAS*, 398, 91
Pulsoni, C., Gerhard, O., Arnaboldi, M., et al. 2018, *A&A*, 618, A94
Rantala, A., Johansson, P. H., Naab, T., Thomas, J., & Frigo, M. 2019, *ApJ*, 872, L17
Riess, A. G., Macri, L. M., Hoffmann, S. L., et al. 2016, *ApJ*, 826, 56
Rusli, S. P., Erwin, P., Saglia, R. P., et al. 2013, *AJ*, 146, 160
Salpeter, E. E. 1955, *ApJ*, 121, 161
Sanders, R. H. & McGaugh, S. S. 2002, *ARA&A*, 40, 263
Schwarz, D. J., Copi, C. J., Huterer, D., & Starkman, G. D. 2016, *Classical and Quantum Gravity*, 33, 184001
Scott, N., Cappellari, M., Davies, R. L., et al. 2013, *MNRAS*, 432, 1894
Smith, R. K., Brickhouse, N. S., Liedahl, D. A., & Raymond, J. C. 2001, *ApJ*, 556, L91

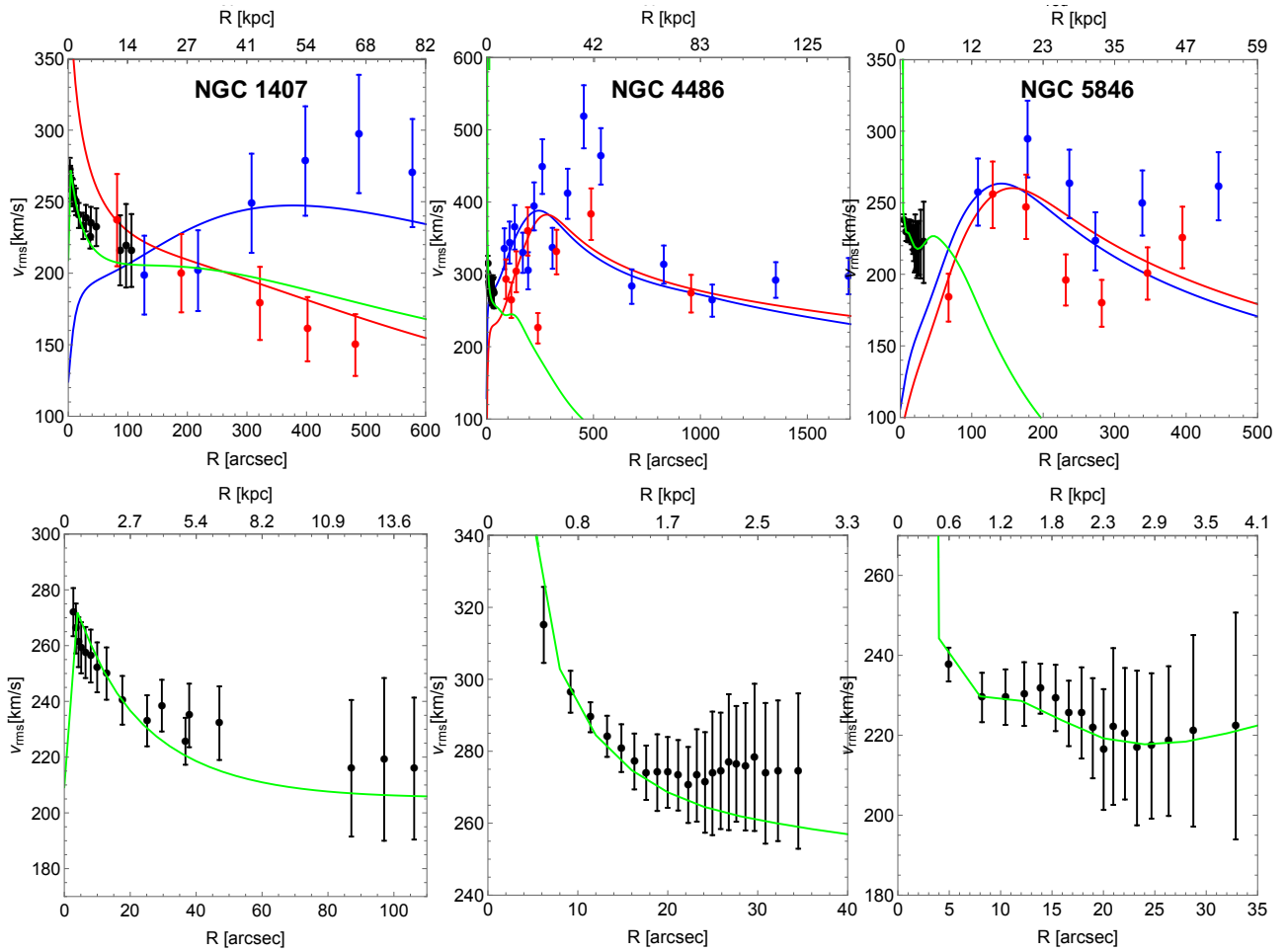


Fig. 11: Same as Fig. 7 for our second MCMC analysis.

- Sollima, A. & Nipoti, C. 2010, MNRAS, 401, 131
Spolaor, M., Forbes, D. A., Hau, G. K. T., Proctor, R. N., & Brough, S. 2008, MNRAS, 385, 667
Strader, J., Romanowsky, A. J., Brodie, J. P., et al. 2011, ApJS, 197, 33
Strigari, L. E., Bullock, J. S., Kaplinghat, M., et al. 2008, Nature, 454, 1096
Tanabashi, M. et al. 2018, Phys. Rev. D, 98, 030001
Thomas, J., Saglia, R. P., Bender, R., Erwin, P., & Fabricius, M. 2014, ApJ, 782, 39
Tulin, S. & Yu, H.-B. 2018, Phys. Rep., 730, 1
van der Marel, R. P. & Franx, M. 1993, ApJ, 407, 525
Verde, L., Treu, T., & Riess, A. G. 2019, Nature Astronomy, 3, 891
Werner, N., McNamara, B. R., Churazov, E., & Scannapieco, E. 2019, Space Sci. Rev., 215, 5
Whitmore, B. C., Sparks, W. B., Lucas, R. A., Macchetto, F. D., & Biretta, J. A. 1995, ApJ, 454, L73
Zhang, Z., Xu, H., Wang, Y., et al. 2007, ApJ, 656, 805
Zhao, H. 1996, MNRAS, 278, 488
Zibetti, S., Charlot, S., & Rix, H.-W. 2009, MNRAS, 400, 1181

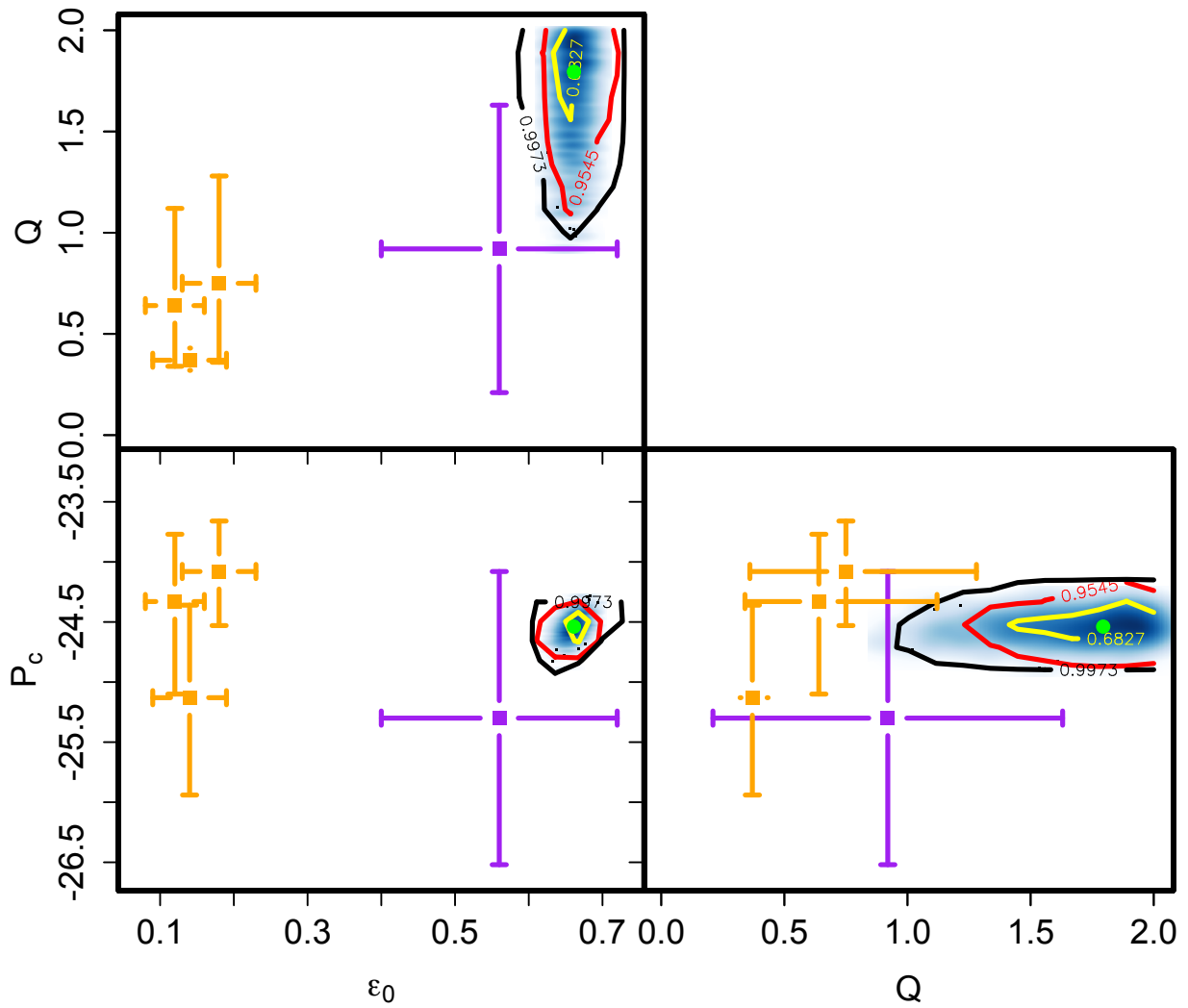


Fig. 12: Permittivity parameters estimated from the three E0 galaxies in our sample (orange squares with error bars) compared with the permittivity parameters estimated by Cesare et al. (2020) from the DMS disk galaxies: the purple squares with error bars show the means of the permittivity parameters found for the individual DMS galaxies, whereas the light blue shaded areas show the posterior distributions of the three permittivity parameters found with an approximate procedure from the entire DMS sample at the same time, with the green dots indicating their median values and the yellow, red, and black contours indicating the 1σ , 2σ , and 3σ levels, respectively.

Appendix A: Derivation of the uncertainties on the root-mean-square velocity dispersions of GCs

We adopt the procedure of Danese et al. (1980) to estimate the uncertainties $\Delta V_{\text{rms}}(R)$ on the values of the root-mean-square velocity dispersion profile $V_{\text{rms}}(R)$ that we compute with Eq. (28). In the reference frame of the centre of mass of the galaxy, the line-of-sight velocity of the i -th GC is

$$v_{\parallel,i} = \frac{V_{\text{rad},i} - V_{\text{sys}}}{1 + V_{\text{sys}}/c}, \quad (\text{A.1})$$

where $V_{\text{rad},i}$ is the observed radial velocity of the GC, V_{sys} is the systemic velocity of the galaxy, and $c = 3 \times 10^5 \text{ km s}^{-1}$ is the speed of light. The three E0 galaxies of our analysis have redshift $z < 0.007$ and we set to 1 the denominator of Eq. (A.1). The variance of the radial velocities of GCs in each radial bin of radius R is

$$\sigma_{\parallel}^2(R) = \frac{1}{N-1} \sum_{i=1}^N v_{\parallel,i}^2, \quad (\text{A.2})$$

where N is the number of GCs in the bin. This equation neglects the errors on V_{rad} and V_{sys} .

The quantity

$$S^2(R) = (N-1) \frac{\sigma_{\parallel}^2(R)}{V_{\text{rms}}^2(R)}, \quad (\text{A.3})$$

is a χ^2_ν random variate with $\nu = N-1$ degrees of freedom. We define S^2_- and S^2_+ with the probability α of having S^2 in the range (S^2_-, S^2_+) . The value $\alpha = 0.68$ defines the upper, indicated with the + sign, and lower, indicated with the - sign, 1σ uncertainty on the dispersion of the radial velocities derived with Eq. (A.2):

$$\Delta\sigma_{\parallel,\pm}^2(R) = \left[\left(\frac{\nu}{S^2_{\mp}(R)} \right)^{1/2} - 1 \right]^2 \sigma_{\parallel}^2(R) + \frac{\overline{\delta_*^2}}{N} \left(1 + \frac{\overline{\delta_*^2}}{2\sigma_{\parallel}^2(R)} \right), \quad (\text{A.4})$$

where $\overline{\delta_*^2}$ is

$$\overline{\delta_*^2} = \frac{\Delta V_{\text{sys}}}{1 + V_{\text{sys}}/c} \quad (\text{A.5})$$

and ΔV_{sys} is the uncertainty on V_{sys} ; $\overline{\delta_*^2} = \Delta V_{\text{sys}}$ in our analysis.

Finally, the upper and lower 1σ uncertainties on $V_{\text{rms}}(R)$ are

$$\Delta V_{\text{rms},\pm}(R) = V_{\text{rms}}(R) \left[\frac{1}{5N} + \left(\frac{\Delta\sigma_{\parallel,\pm}(R)}{\sigma_{\parallel}(R)} \right)^2 \right]^{1/2}. \quad (\text{A.6})$$

In our analysis, we use the symmetrised uncertainty

$$\Delta V_{\text{rms}}(R) = \frac{\Delta V_{\text{rms},-}(R) + \Delta V_{\text{rms},+}(R)}{2}. \quad (\text{A.7})$$